JOURNAL OF PROPULSION AND POWER
Vol. 21, No. 6, November–December 2005

Linear Analysis of a Liquid-Film Combustor

William A. Sirignano,* Simone Stanchi,† and Randall Imaoka†
University of California, Irvine, Irvine, California 92697

Steady-state axisymmetric combustion in a cylindrical chamber with the liquid fuel introduced through a wall film is analyzed. For the miniature combustor of interest, the swirling core flow of air, fuel vapor, and products operates in the laminar range. Under the condition of unitary Lewis number, the analysis of the scalar fields takes advantage of the existence of a linear combination of the scalar properties, known as the super scalar, which is spatially uniform. The base flow is assumed to have constant density and to be either a fully developed flow or a plug flow. Perturbations account separately for swirl effects, Stefan flow, and density variations. Therefore, some linearization becomes helpful. The effects of each perturbation type on the velocity fields and scalar fields are determined. The motion in the liquid film is coupled to the core gas motion. The diffusion flame character is portrayed. Vaporization rates and burning rates are determined; the effects of radial velocity perturbations, due to swirl and Stefan flow, and of the density variations on the transport, vaporization, and burning rates are determined. The analysis yields closed-form solutions in terms of eigenfunction expansions. Series solutions are found to certain ordinary differential equations describing radial variations in the dependent variables. Large Damkohler number solutions are calculated as functions of Reynolds number and Peclet number, showing strong dependencies. Methanol and heptane fuels are considered. Limits of high Peclet number are also examined. The results allow for the prediction of required chamber length for given chamber diameter, inlet flow conditions, liquid-fuel physicochemical properties, initial fuel temperature, and overall mixture ratio. The feasibility of the liquid-film concept, which has been demonstrated in the laboratory, is supported theoretically.

I. Introduction

COMBUSTION has the potential to provide simultaneously high-power density and high-energy density; these parameters make it more attractive than batteries and fuel cells for applications in which weight is an issue, for example, flight or mobile power sources. Therefore, it is important to study this method of power generation at small scale. The microgas turbine[1] (combustor volume 0.04 cm^3), the mini- (0.078 cm^3 displacement) and micro- (0.0017-cm^3 displacement) rotary engine,[2] the microrocket[3,4] (0.1-cm^3 combustion chamber), and the micro-Swiss-roll burner[5] are examples of such studies. These devices are not yet sufficiently efficient to compete with the best batteries; however, the feasibility of internal combustion as a miniature power source has been shown. The major challenge for all miniature-combustor designs is the increasing surface-to-volume ratio S/V with decreasing size. Combustor-wall temperatures are kept fairly low due to material considerations and high S/V usually produces flame quenching, attracting researchers to quench-resistant fuels, for example, hydrogen, high-preheat concepts (as with the Swiss-roll burner), or catalytic surfaces.[6] Kyritsis et al.[7] have some interesting approaches using catalysts and electrospraying. Much of the earlier research in compact energy and power sources has derived from Defense Advanced Research Projects Agency programs in palm power and portable power. These programs are often device based and constrained by specific target applications, making it difficult to study the fundamentals of potentially new combustion regimes governed by small physical scales and high surface to volume ratios. A useful overview of those studies is given by Fernandez-Pello[8] and by Walther and Fernandez-Pello.[9]

Recent studies[10–13] indicate that the strategy of vaporizing liquid fuel from a film on the combustor wall offers significant advantages over spray vaporization for miniature combustors. The liquid-fuel-film minimizes heat loss to the wall, inhibits flame quenching, and keeps the temperature of the wall material low. These findings are based on dimensional analysis, order-of-magnitude analysis, and experiments. The experimental observations and measurements[10,12,13] provide the proof of concept for a University of California patent application.

This paper presents an analytical treatment of the governing partial differential equations. Although the film-combustor concept is not limited to continuous combustors or to any particular geometry, we consider here steady continuous combustion in a circular-cylindrical chamber. The mixing and reaction occurs, therefore, in a gas surrounded by a liquid-fuel film. The analytical perturbation approach taken here offers some advantage over the direct numerical integration of the Navier–Stokes equations for the reacting flow. The separate effects of the base axial flow, the induced swirl, the Stefan flow, and the expanding gas flow on the mixing and chemical reaction can be evaluated. The effects of different parameters can be more readily evaluated, for example, fuel heating value, fuel volatility (boiling point and latent heat of vaporization), mass stoichiometric ratio, inflow oxygen concentration, Peclet and Reynolds numbers, swirl ratio, inflow velocity profiles, and chamber length. A disadvantage is that the interesting practical range for a few of the parameters extends beyond the applicable domain for small perturbation theory; as a consequence, some results should be viewed as having qualitative value rather than quantitative value. Any unsteadiness or three dimensionality that might result from incipient turbulence at the higher Reynolds numbers or from the inflows of air or liquid flow is neglected.

The major assumptions and governing equations are presented in the next section. The super-scalar approach is used to determine the flame temperature (in the limit of infinite chemical-kinetic rate) and surface temperature (before the field equations are solved) as functions of the heat per unit mass transferred to the liquid surface. The liquid-phase analysis is briefly discussed in Sec. III, in which it is shown that, for certain cases, the liquid-phase field can be determined before the gas phase is resolved in detail. Solutions for the axial-velocity field and gas scalar field are found in Secs. IV and V, respectively. In Sec. VI, the solution of the tangential-velocity component that results from the swirling inflow is addressed, whereas in Sec. VII the analysis of the radial velocity induced by the swirl is presented. The Stefan-flow perturbation (caused by the blowing

---

Received 22 October 2004; revision received 7 March 2005; accepted for publication 8 March 2005.

*Professor, Mechanical and Aerospace Engineering; sirignan@uci.edu. Fellow AIAA.

†Research Assistant, Mechanical and Aerospace Engineering.

effect of vaporization at the liquid/gas interface) and the effect of the gas expansion due to chemical energy release are described in Sec. VIII. The modification of the vaporization rate and burning rate due to combined radial velocity is discussed in Sec. IX. Some concluding remarks are made in Sec. X.

II. Assumptions and Governing Equations

The liquid fuel is injected along the cylindrical wall of the combustion chamber and is spread in a wall film by the shearing action of the gas. The gas flows axially but is injected with a weak swirl component to spread the liquid film and to provide the centrifugal effect that keeps the film on the wall. The swirl is not strong enough in this model to create a recirculation zone.

The liquid is assumed to be a single compound, for example, heptane or methanol. Consider the gas phase that is surrounded by the liquid-fuel film to have a laminar multicomponent flow with viscosity, Fourier heat conduction, Fickian mass diffusion, and one-step oxidation kinetics. Diffusivities for all species are assumed identical, the Lewis number value is unity, radiation will be neglected, and kinetic energy is neglected in comparison to thermal energy so that, with regard to the energetics, pressure is considered uniform over the space, although the pressure gradient can be significant in the momentum balance (small Mach number). Both steady and unsteady scenarios are discussed in the first few sections. Later, the analysis focuses on steady flows.

The liquid-film thickness will be much smaller than the chamber radius because the fuel mass flow rate is an order of magnitude smaller than the airflow rate and the liquid density is orders of magnitude larger than the gas density.

The thermal and mass diffusivities are equal so that the Lewis number $Le = 1$ and $\rho D = \lambda / c_p$. With the one-step reaction, the various reaction rates are proportioned by the stoichiometric ratios, $\dot{w}_F = \nu \dot{w}_O = -\nu \dot{w}_P/(1+\nu)$, where ν is the stoichiometric fuel-to-oxidizer mass ratio. The species equations governing the mass fractions Y_i become

$$L(Y_i) \equiv \rho \frac{\partial Y_i}{\partial t} + \rho \boldsymbol{u} \cdot \nabla Y_i - \nabla \cdot (\rho D \nabla Y_i) = \rho \dot{w}_i, \qquad i = F, O, P \tag{1}$$

The energy equation is written as

$$L(h) \equiv \rho \frac{\partial h}{\partial t} + \rho \boldsymbol{u} \cdot \nabla h - \nabla \cdot (\rho D \nabla h) = -\rho \dot{w}_F Q + \frac{\partial p}{\partial t} \tag{2}$$

where the sensible enthalpy h is given as

$$h = \sum_i Y_i \int_{T_{\mathrm{ref}}}^{T} c_{pi}(T')\,\mathrm{d}T' = \sum_i Y_i h_i = \int_{T_{\mathrm{ref}}}^{T} c_p(T')\,\mathrm{d}T' \tag{3}$$

with

$$c_p \nabla T = \nabla h - \sum_i h_i \nabla Y_i \tag{4}$$

We define two Shvab-Zel'dovich variables for the gas phase: $\alpha^{(1)} = h + \nu Q Y_O$ and $\alpha^{(2)} = Y_F - \nu Y_O$. Consider now that pressure is steady, although other variables can vary with time. Equations (1) and (2) yield

$$L\big(\alpha^{(1)}\big) = 0, \qquad L\big(\alpha^{(2)}\big) = 0 \tag{5}$$

At the outflow boundaries, the spatial normal derivatives of the primitive variables can be set to zero in standard fashion. This assumes that mixing and combustion are completed before outflow. Therefore,

$$\frac{\partial \alpha^{(i)}}{\partial n} = 0, \qquad i = 1, 2 \tag{6}$$

where n is the coordinate measuring normal distance (positive into the gas) from the boundary.

At the upstream inflow boundary, $\alpha^{(1)}$ and $\alpha^{(2)}$ each maintain uniform but possibly time-varying values. Thus,

$$\alpha^{(i)} = \alpha^{(i)}_{\infty}(t), \qquad i = 1, 2 \tag{7}$$

At the vaporizing liquid surface, the combustion product gas does not penetrate, so that Stefan advection and diffusion balance there. The oxidizer gas is consumed in a surrounding flame before it reaches the liquid surface so that the oxidizer mass fraction is zero at and near the surface. For the fuel vapor species, we have

$$\dot{m}(1 - Y_{Fs}) = -\rho D \left.\frac{\partial Y_F}{\partial n}\right)_s \tag{8a}$$

where $\dot{m}$ is the vaporization rate per unit surface area and n is the normal coordinate. The subscript s implies conditions at the liquid surface. In another surface condition, the energy flux from the gas to the surface (due to combined heat conduction and energy transfer by mass diffusion) is balanced by the combination of the heat required for vaporization and the heat conducted to the liquid interior. When Eqs. (4) and (8a) are used with the unitary Lewis number condition, the surface condition becomes

$$\left.\frac{\partial h}{\partial n}\right)_s = -\frac{L_{\mathrm{eff}}}{1 - Y_{Fs}} \left.\frac{\partial Y_F}{\partial n}\right)_s = \frac{\dot{m} L_{\mathrm{eff}}}{\rho D} \tag{8b}$$

The effective heat of vaporization L_{eff} combines the actual latent heat of vaporization with the heat per unit mass conducted into the liquid interior, $L_{\mathrm{eff}} = L + \dot{q}_\ell / \dot{m}$, where $\dot{q}_\ell$ is the heat flux to the interior per unit surface area and $\dot{m}$ is the vaporization mass flux per unit surface area.[14]

From Eq. (8a), we can deduce that the vaporization rate per unit surface area is given by

$$\dot{m} = -\left[\frac{\rho D}{(1 - Y_{Fs})}\right] \left.\frac{\partial \alpha^{(2)}}{\partial n}\right)_s \tag{9}$$

The following super-scalar has been contrived[15] as a certain linear combination of primitive scalar variables:

$$\begin{aligned} S &= \alpha^{(1)} + [L_{\mathrm{eff}}/(1 - Y_{Fs})]\alpha^{(2)} = h \\ &\quad + \nu\{Q - [L_{\mathrm{eff}}/(1 - Y_{Fs})]\}Y_O + [L_{\mathrm{eff}}/(1 - Y_{Fs})]Y_F \end{aligned} \tag{10}$$

Here L_{eff} and Y_{Fs} each have the same instantaneous values uniformly across all of the liquid surfaces in the particular configuration. Y_{Fs} is a function of the surface temperature T_s through the phase-equilibrium law,

$$Y_{Fs} = Y_{Fs}(T_s) \tag{11}$$

In the steady state, the time derivatives in Eqs. (1) and (2) are zero and the parameters in boundary conditions (7) and (9) are steady. In the quasi-steady state, the time derivatives in Eqs. (1) and (2) are negligible compared to other terms in the equations although parameters in boundary conditions (7) and (9) may be time varying. The thermal behavior of the liquid may be unsteady if the surface temperature is steady or quasi steady. Equation (10) when subjected to Eqs. (5) and boundary conditions (6), (7), and (9) produces the spatially uniform value

$$\begin{aligned} S = S_\infty(t) &= h_\infty + \nu[Q - L_{\mathrm{eff}}/(1 - Y_{Fs})]Y_{O\infty} \\ &\quad + L_{\mathrm{eff}} Y_{F\infty}/(1 - Y_{Fs}) = h_f \end{aligned} \tag{12}$$

where subscript f corresponds to the flame position where $Y_O = Y_F = 0$. This result is valid if the primitive variables h_∞, $Y_{O\infty}$, and $Y_{F\infty}$ vary over the boundary provided that the linear combination S_∞ is instantaneously uniform.

Two possibilities are allowed: 1) No fuel vapor exists on the oxygen (upstream) side of the flame so that $Y_{F\infty} = 0$ and a pure diffusion flame occurs. 2) Fuel vapor exists on both sides of each flame in the configuration so that both a premixed character and a diffusion character exist for the flame(s). Consequently, Eq. (12) implies that

$$\frac{h_\infty - h_s + \nu Q Y_{O\infty}}{L_{\text{eff}}} = \frac{Y_{Fs} - Y_{F\infty} + \nu Y_{O\infty}}{1 - Y_{Fs}} \equiv B \qquad (13)$$

Thus, Eq. (13) defines the well-known Spalding transfer number B for the $Le = 1$ case. More important, Eq. (13) together with the enthalpy–temperature relationship $h(T)$ and the phase equilibrium law $Y_{Fs} = Y_{Fs}(T_s)$ serve as boundary conditions on (steady or unsteady) heat transfer in the liquid because the effective latent heat of vaporization, $L_{\text{eff}} = L + \dot{q}_\ell/\dot{m}_f$, contains the normal temperature gradient on the liquid side of the interface.[14] Equation (13) determines the surface temperature T_s and the surface mass fraction Y_{Fs} as functions of fuel properties, inflow conditions, and L_{eff}. Coupled with the liquid-phase heat transfer problem, T_s and Y_{Fs} are absolutely determined as functions of time. These surface values are affected by the details of the configuration or of the hydrodynamics and transport phenomena only through L_{eff}.

In the limit of infinite reaction rate, the flame becomes a sheet of zero thickness at which $Y_O = Y_F = 0$. Equation (12) then yields a formula for the limiting flame temperature T_f,

$$h(T_f) = h(T_\infty) + \nu[Q - L_{\text{eff}}/(1 - Y_{Fs})]Y_{O\infty} + [L_{\text{eff}}/(1 - Y_{Fs})]Y_{F\infty} = h(T_s) + \{L_{\text{eff}}/[1 - Y_{Fs}(T_s)]\}Y_{Fs}(T_s) \qquad (14)$$

For constant specific heat, the limiting flame temperature is given by

$$\frac{T_f}{T_\infty} = 1 + \nu\left(\frac{Q}{c_p T_\infty} - \frac{L_{\text{eff}}/c_p T_\infty}{1 - Y_{Fs}}\right)Y_{O\infty} + \frac{L_{\text{eff}}/c_p T_\infty}{1 - Y_{Fs}}Y_{F\infty} = \frac{T_s}{T_\infty} + \frac{L_{\text{eff}}/c_p T_\infty}{1 - Y_{Fs}(T_s)}Y_{Fs}(T_s) \qquad (15)$$

Flame temperature as well as liquid surface temperature depend on the dynamics or configuration only through L_{eff}. Particularly, they depend on the inflow conditions, the fuel properties, and the heat per unit mass transferred to the liquid.

It has been shown[15] that the results of this section apply much more broadly than to continuous combustion in a cylindrical chamber.

III. Liquid-Phase Thermal Analysis

The uniformity of the super-scalar S over the gas phase does require that L_{eff} is instantaneously uniform over the liquid surface. The latent heat of vaporization L is a fuel property and, therefore, will be uniform and constant. The uniformity of the heat flux to the interior per unit mass flux $\dot{q}_\ell/\dot{m}$ is a more demanding requirement. It can be satisfied in various situations.[14] In one situation where the wet-bulb temperature has been reached, $\dot{q}_\ell = 0$. In a second situation where a thin quasi-steady thermal layer exists in the liquid near the surface, $\dot{q}_\ell/\dot{m} = c_\ell(T_s - T_O)$, where c_ℓ is the liquid specific heat and T_o is the liquid interior temperature. Because the liquid-phase Prandtl number is much larger than unity, we can expect the thermal layer at the liquid surface to be much thinner than the liquid viscous layer. Then, L_{eff} has a uniform value in either of those two situations and Eq. (13) together with an equation of state for h and a phase-equilibrium law immediately yield surface values. Then, Eq. (14) or (15) can readily give the limiting flame temperature. Furthermore, the details of the liquid flow do not modify the magnitude of L_{eff} in these situations with uniform surface temperature and thin thermal layer.

In this analysis, it shall be assumed that a thin quasi-steady thermal liquid layer exists adjacent to the surface. In particular, the layer thickness will be taken to be smaller than the liquid-film thickness, and then the film thickness is not an interesting parameter in the heat transfer process. Also, the details of the liquid motion are not important for heat transfer. The solid/liquid interface can be considered as adiabatic under this situation. Note that L_{eff} remains constant as the characteristic diffusion length varies with downstream distance because $\dot{q}_\ell$ varies in proportion to $\dot{m}$.

More information, beyond the scope of this analysis, about flames in gaseous diffusion layers adjacent to vaporizing liquid films or pools may be found in the literature.[16–24] Emmons[16] considered the similar solution of diffusion and reaction with forced gas motion above a flat liquid surface without liquid motion or liquid-phase temperature gradients. Smirnov[17] extended the Emmons two-dimensional, steady analysis and considered liquid motion and heating in a thick liquid film where the solid-wall interface played no role. The effects of unsteady flame development, finite liquid pool depth, surface-tension driven flow, and buoyancy in both phases have been considered in two-dimensional,[18–21] axisymmetric,[22] and three-dimensional[23,24] configurations.

IV. Fluid Dynamics Analysis

Consider steady, viscous, laminar axisymmetric flow using a cylindrical coordinate system. Swirl will be allowed. Here, u, v, and w are the x, r, and θ components of velocity, respectively. The continuity and momentum equations are[25]

$$\frac{\partial}{\partial x}(\rho u) + \frac{1}{r}\frac{\partial}{\partial r}(\rho v r) = 0 \qquad (16)$$

$$\rho u\frac{\partial u}{\partial x} + \rho v\frac{\partial u}{\partial r} + \frac{\partial p}{\partial x} = \frac{1}{r}\frac{\partial}{\partial r}\left(\mu r\frac{\partial u}{\partial r}\right) + \frac{\partial}{\partial x}\left(\mu\frac{\partial u}{\partial x}\right) + \left[\frac{\partial \mu}{\partial x}\frac{\partial u}{\partial x} + \frac{\partial \mu}{\partial r}\frac{\partial v}{\partial x}\right] + \mu\frac{\partial}{\partial x}(\nabla\cdot\boldsymbol{u}) - \frac{2}{3}\frac{\partial}{\partial x}(\mu\nabla\cdot\boldsymbol{u}) \qquad (17)$$

$$\rho u\frac{\partial v}{\partial x} + \rho v\frac{\partial v}{\partial r} - \frac{\rho w^2}{r} + \frac{\partial p}{\partial r} = \frac{1}{r}\frac{\partial}{\partial r}\left(\mu r\frac{\partial v}{\partial r}\right) - \frac{\mu v}{r^2} + \frac{\partial}{\partial x}\left(\mu\frac{\partial v}{\partial x}\right) + \frac{\partial \mu}{\partial x}\frac{\partial u}{\partial r} + \frac{\partial \mu}{\partial r}\frac{\partial v}{\partial r} - \frac{2}{3r}\frac{\partial}{\partial r}(\mu r\nabla\cdot\boldsymbol{u}) + \frac{2\mu}{3}\frac{\nabla\cdot\boldsymbol{u}}{r} \qquad (18)$$

$$\rho u\frac{\partial w}{\partial x} + \rho v\frac{\partial w}{\partial r} + \frac{\rho v w}{r} = \frac{1}{r}\frac{\partial}{\partial r}\left[\mu r^2\frac{\partial}{\partial r}\left(\frac{w}{r}\right)\right] + \frac{\partial}{\partial x}\left(\mu\frac{\partial w}{\partial x}\right) + \mu\frac{\partial}{\partial r}\left(\frac{w}{r}\right) \qquad (19)$$

Note that these equations will apply in both the gas and liquid. Bulk viscosity has been set to zero. Whereas the velocity, normal stress, and shear stress will be continuous across the liquid/gas interface, discontinuities in density and viscosity will occur there.

The flowfield will be considered to be a fully developed laminar flow with certain perturbations. The perturbations result from the combustion process (variations in density and temperature), imposed swirl, Stefan convection due to liquid film vaporization, and differences between initial conditions and the developed flow asymptote. Although the base flow without these perturbations is fully developed, it still differs from classical fully developed pipe flow because of the liquid wall film. The flow can be represented as

$$\begin{aligned} u &= u_0(r) + u_1(r, x) + - - - \\ v &= v_1(r, x) + - - - \\ w &= w_1(r, x) + - - - \\ p &= p_0(x) + p_1(r, x) + - - - \\ \rho &= \rho_0 + \rho_1(r, x) + - - - \\ \mu &= \mu_0(r) + \mu_1(r, x) + - - - \end{aligned} \qquad (20)$$

where terms with subscript $n \geq 1$ are considered as perturbations to the basic fully developed flow, which is represented with subscript 0. The assumption of low Mach number (negligible compressibility), weak swirl, and weak Stefan convection are reasonable. The strongest assumption is the consideration of density variation due to temperature variation as a perturbation, allowing the first approximation of density ρ_0 to be a constant.

The series (20) is substituted into Eqs. (16–19) and separated according to the order of the terms. The first approximation from

Eq. (16) yields the result that u_0 depends only on the radial position r.

The lowest-order approximation from Eq. (17) yields that

$$\frac{1}{r}\frac{\mathrm{d}}{\mathrm{d}r}\left(\mu_0 r\frac{\mathrm{d}u_0}{\mathrm{d}r}\right)=\frac{\mathrm{d}p_0}{\mathrm{d}x} \tag{21}$$

The first approximation for the tangential velocity component results from Eq. (19). We find that

$$\rho_0 u_0\frac{\partial w_1}{\partial x}=\frac{1}{r}\frac{\partial}{\partial r}\left[\mu_0 r^2\frac{\partial}{\partial r}\left(\frac{w_1}{r}\right)\right]+\mu_0\frac{\partial}{\partial r}\left(\frac{w_1}{r}\right)+\frac{\partial}{\partial x}\left(\mu_0\frac{\partial w_1}{\partial x}\right) \tag{22}$$

The next equations resulting from the separation of Eqs. (16) and (17) plus the first approximation from Eq. (18) yield a system of three equations governing the perturbations u_1, v_1, ρ_1, and p_1. See Eqs. (60a–60c). An equation of state will connect ρ_1 and p_1. These terms will not be considered in the lowest-order analysis. The higher-order equations are discussed and solved later in Sec. VII.

First, a solution of Eq. (21) for u_0 is developed. The viscosity will be assumed to be constant through each phase with a discontinuity at the interface. Both velocity and shear stress will be continuous across the interface, whereas the normal derivative of velocity is discontinuous. Equation (21) indicates that the radial profile of u_0 is a parabola in each phase. It also implies that the pressure gradient $\partial p_0/\partial x$ is a constant. The combustor chamber has constant radius R, whereas the liquid/gas interface has radius R_i. Because the liquid film thickness is much smaller than the radius R_i, the value R_i can be assumed constant from the gas-phase perspective. In fact, $R_i \approx R$. However, the variation of R_i is significant from the liquid-phase perspective. Equation (21) is subject to a no-slip condition at the wall ($r = R$), a symmetry condition at $r = 0$, continuous velocity at $r = R_i$, continuous shear stress at $r = R_i$, and continuous pressure at $r = R_i$. The result is that

$$u_0=\left[R_i^2\left(1-\frac{\mu_\ell}{\mu_g}\right)-R^2+\frac{\mu_\ell}{\mu_g}r^2\right]\frac{1}{4\mu_\ell}\frac{\mathrm{d}p_0}{\mathrm{d}x} \tag{23a}$$

for $0 \le r \le R_i$ and

$$u_0=(r^2-R^2)\frac{1}{4\mu_\ell}\frac{\mathrm{d}p_0}{\mathrm{d}x} \tag{23b}$$

for $R_i \le r \le R$ (liquid phase). Note that the pressure gradient will be negative while the velocity is positive. Also, as $R_i \to R$, Eq. (23a) yields the well known single-phase result for fully developed pipe flow.

The centerline velocity is given by

$$u_c=u_0(0)=\left[R_i^2\left(1-\frac{\mu_\ell}{\mu_g}\right)-R^2\right]\frac{1}{4\mu_\ell}\frac{\mathrm{d}p_0}{\mathrm{d}x} \tag{24}$$

Equations (23a) and (23b) can be nondimensionalized,

$$u_0/u_c=1-\varepsilon^2\tilde{r}^2 \tag{25a}$$

for $0 \le \tilde{r} \le R_i/R$, and

$$\frac{u_0}{u_c}=\frac{1-\tilde{r}^2}{1-(1-\mu_\ell/\mu_g)(R_1/R)^2}=\varepsilon^2\frac{\mu_g}{\mu_\ell}(1-\tilde{r}^2) \tag{25b}$$

for $R_i/R \le \tilde{r} \le 1$, where $\tilde{r} \equiv r/R$, and

$$\varepsilon^2 \equiv \frac{\mu_\ell/\mu_g}{1-(1-\mu_\ell/\mu_g)(R_i/R)^2} \tag{25c}$$

The parabolic profile is characteristic of a fully developed laminar flow in the gas core. We shall also examine a case where the core gas flow is represented as a plug flow; this represents a situation where the flow is just beginning to develop (or a less practical situation where the liquid viscosity is negligible). It is characterized by $\varepsilon = 0$, which implies that the gaseous viscous layer at the liquid surface is very thin, that is, large gas-phase Reynolds number for the developing flow, and/or the liquid viscosity is negligible, that is, large liquid-phase Reynolds number. The approximation given by Eq. (21) does not apply in this limit; the gas-phase pressure drop becomes negligible. The core flow in this plug-flow limit has a flat profile that matches the inflow profile. Here $\varepsilon = 1$ is the limit where the liquid-film thickness is negligible. For the calculations in this paper, $\tilde{r}_i = 0.98$ is taken. The viscosity ratio is taken as $\mu_\ell/\mu_g = 2.21631$ so that, for the parabolic-velocity-profile calculations, $\varepsilon = 1.01105$ is obtained from Eq. (25c).

V. Scalar Analysis

Consider now the solutions for gas temperature and mass fractions for the $Le = 1$ condition. The super-scalar S given by Eq. (10) can be determined as indicated earlier. Consistent with the neglect of Stefan convection, the factor $(1 - Y_{Fs})$ in boundary conditions (8) and (9) and in the denominators of Eq. (10) is replaced by one. If Eq. (5) is solved for the second Shvab-Zel'dovich variable $\alpha^{(2)}$, knowledge of S will immediately yield $\alpha^{(1)}$. Then, assuming infinite chemical kinetic rate, we can determine temperature and mass fractions.

For convenience, we will add a constant to $\alpha^{(2)}$ and then normalize it so that it becomes zero at the liquid interface and has unitary value at the inflow,

$$\alpha=\frac{\left[Y_F-\nu Y_O-Y_{Fs}\right]}{\left[-\nu Y_{O\infty}-Y_{Fs}\right]} \tag{26}$$

Recall that Y_{Fs} and T_s can be determined a priori as already indicated. The value of α at the flame will be given by setting the oxidizer and fuel-vapor mass fractions in Eq. (26) to zero. Then, $\alpha_f = Y_{Fs}/[\nu Y_{O\infty} + Y_{Fs}]$. Thus, whereas the line for any particular value of α for a contour plot in the r–z plane does not depend on the specific fuel or oxidizer, the particular line that gives the flame position in the limit of infinite kinetics does depend on the choice of fuel and oxidizer. The contours of the primitive variables such as temperature and mass fraction will also depend on the fuel and oxidizer.

Equation (5) can be recast in steady axisymmetric form using the cylindrical coordinates and the lowest approximations from Eq. (20). Here u_c and R are used to nondimensionalize time and space coordinates. The diffusivity D is considered to be constant. The lowest-order approximation for α is given by

$$Pe(1-\varepsilon^2\tilde{r}^2)\frac{\partial\alpha}{\partial\tilde{x}}=\frac{1}{\tilde{r}}\frac{\partial}{\partial\tilde{r}}\left(\tilde{r}\frac{\partial\alpha}{\partial\tilde{r}}\right)+\frac{\partial^2\alpha}{\partial\tilde{x}^2} \tag{27}$$

where the Peclet number is given by $Pe = u_c R/D$. Solutions will be sought using eigenfunction expansions. Separation of the variable α yields

$$\alpha=\Theta(\tilde{r})e^{-k\tilde{x}} \tag{28}$$

where Θ is governed by the ordinary differential equation

$$\Theta''+(1/\tilde{r})\Theta'+\lambda^2\left(1-\varepsilon_*^2\tilde{r}^2\right)\Theta=0 \tag{29}$$

The boundary conditions on Eq. (29) are that $\Theta(\tilde{r}_i) = 0$ and the solution remains finite everywhere. Here $\lambda^2 \equiv Pe\,k + k^2$, or, taking only the positive value, $k = \frac{1}{2}(Pe^2 + 4\lambda^2)^{\frac{1}{2}} - \frac{1}{2}Pe$. Also, $\varepsilon_* = \varepsilon/(1 + k/Pe)^{\frac{1}{2}}$. A Peclet number value that is large compared to unity implies that axial diffusion is dominated by both axial advection and radial diffusion. As $Pe \to \infty$, the finite ε_* becomes independent of Peclet number and Eq. (29) and its boundary conditions indicate that Θ and λ become independent of Peclet number. For $\varepsilon = 0$, Θ and λ are independent of Peclet number for any Peclet number value. Then, for $Pe \to \infty$ and for any ε value, $k = \lambda^2/Pe$, and Eq. (28) indicates that the dependencies of α on $\tilde{x}$ and Peclet number collapse to an exponentially decaying dependence on $\tilde{x}/Pe$.

When $\varepsilon = 0$, Eq. (29) becomes Bessel's equation of zero order. This limit can be used when a plug flow is considered; the value of u_c in the nondimensionalization scheme should be replaced by the uniform velocity given by u_0. Graetz has solved heat and mass transfer problems of this type for both fully developed single-phase flow, $\varepsilon = 1$, and plug flow, $\varepsilon = 0$. Review of the Graetz work and related works by Nusselt and others may be found in Refs. 26 and 27. The current work differs from Graetz's work primarily through the effect of the liquid wall film and secondarily through the inclusion of diffusion in the main flow direction as well as in the lateral direction. Prior workers have extended the Graetz problem to include multidirectional transport.[27] Note $\varepsilon = 0$ with finite Peclet number implies that the viscous flow is completely undeveloped dynamically but the scalar diffusion layer is developing.

Equation (29) has a regular singular point at $\tilde{r} = 0$. Two series solutions can be found; one is analytic and the other has a logarithmic singularity at the origin. We discard the second solution because the solution is constrained to remain finite. The recursive relation for the coefficients in the analytic series connects three sequential coefficients. A simpler recursive relation connecting only two coefficients is found via transformation of the dependent variable by extracting an exponential term. Equation (29), with the conditions that the solution becomes zero at the liquid interface ($\tilde{r} = R_i/R$) and remains finite in the domain, presents a Sturm–Liouville problem (see Ref. 28) when ε_* has a uniform value for all n. Thus, an infinite number of eigenfunctions and eigenvalues are produced, namely,

$$\Theta_n(\eta, \beta_n) = \exp\left(-\frac{\beta_n \eta^2}{4}\right) \sum_{m=0}^{\infty} a_{2m}(\beta_n)\eta^{2m} \tag{30a}$$

where

$$a_{2m}(\beta_n) = \left(-\tfrac{1}{4}\right)^m \left\{ \overset{m-1}{\underset{p=0}{\pi}} (1 - 2p\beta_n)/[m!]^2 \right\} \tag{30b}$$

with $a_0 = 1$ so that $\Theta_n(0, \beta_n) = 1$. The definitions have been made that

$$\eta \equiv \frac{2\varepsilon_* \sqrt{1 + \beta_n}\tilde{r}}{\beta_n}$$

$$\beta_n \equiv 1 \bigg/ \left(\frac{\lambda_n}{2\varepsilon_*} - 1\right) = 1 \bigg/ \left(\frac{\sqrt{Pek_n + k_n^2}}{2\varepsilon_*} - 1\right) \tag{30c}$$

where n is a positive integer, varying from one to infinity. The subscript n is now used for both λ and k.

The values of β_n are determined by finding the points where the undulating function Θ becomes zero for $\tilde{r} = R_i/R$. Then β_n values are given by

$$\exp\left[-\frac{\varepsilon_{**}^2(1 + \beta_n)}{\beta_n}\right] \sum_{m=0}^{\infty} a_{2m}(\beta_n) \left[\frac{2\varepsilon_{**}\sqrt{1 + \beta_n}}{\beta_n}\right]^{2m} = 0 \tag{31}$$

where

$$\varepsilon_{**} = \varepsilon_* \left(\frac{R_i}{R}\right) = \frac{\varepsilon(R_i/R)}{(1 + k_n/Pe)^{\frac{1}{2}}} \tag{32}$$

For the case where $Pe \gg 1$, the dependence of ε_{**} or ε_* on k_n is weak. Nevertheless, because k_n depends on β_n through λ_n, an iterative solution of Eqs. (30c), (31), and (32) is required. The Sturm–Liouville theory guarantees the generation of a complete orthogonal set of functions only when ε_* is independent of n (see Refs. 28 and 29). Equation (32) shows that with finite ε this occurs when Peclet number becomes infinite. We shall consider that the Peclet number is at least an order magnitude greater than any interesting nondimensional wave number. Consequently, we assume that the expansion of a function in a series of the eigenfunctions given by Eq. (30) is a decent approximation for large Peclet number. For a thin liquid heptane film ($\tilde{r}_i = 0.98$), we find that $\varepsilon = 0.97$. Thus, with $Pe = 1000$, we obtain the eigenvalues listed in Table 1. For the large value of Peclet number in this calculation, the dependence of the numbers in the table on Peclet number is very weak. Note that other researchers[30,31] have developed a complete orthogonal set of eigenfunctions from Eq. (27) for a related problem that differs from the present problem in terms of the boundary conditions. For their problem, they obtain both positive and negative values of the eigenvalue k_n. Unlike our problem, they do have interest in the solution behavior upstream of the plane $\tilde{x} = 0$.

Table 1 Eigenvalues: λ_n for $Pe = 1000$

n	λ_n	n	λ_n
1	2.75373	27	107.68062
2	6.78922	28	111.68058
3	10.84194	29	115.67670
4	14.89643	30	119.66894
5	18.95072	31	123.65717
6	23.00428	32	127.64133
7	27.05682	33	131.62132
8	31.10819	34	135.59706
9	35.15826	35	139.56851
10	39.20687	36	143.53556
11	43.25389	37	147.49818
12	47.29918	38	151.45629
13	51.34261	39	155.40984
14	55.38403	40	159.35876
15	59.42332	41	163.30302
16	63.4603	42	167.24256
17	67.4949	43	171.17740
18	71.5270	44	175.10739
19	75.5564	45	179.03259
20	79.5830	46	182.95296
21	83.60669	47	186.86856
22	87.62729	48	190.77930
23	91.64475	49	194.68468
24	95.65893	50	198.58548
25	99.66970	51	202.47377
26	103.67697	52	206.34955

When $\varepsilon = 0$, $\Theta_n = J_0(\lambda_n \tilde{r})$, which is the Bessel function of the first kind and zero order. Equation (29) and its boundary conditions do form a Sturm–Liouville problem for any Peclet number value in this $\varepsilon = 0$ limit.

Once the values of β_n are known, the functions Θ_n can be determined, and the general solution to Eq. (27) that satisfies the boundary conditions at the liquid interface is

$$\alpha = \frac{[Y_F - \upsilon Y_O - Y_{Fs}]}{[-\upsilon Y_{O\infty} - Y_{Fs}]} = \sum_{n=1}^{\infty} c_n \Theta_n(\tilde{r}) \exp(-k_n \tilde{x}) \tag{33}$$

Again, this is strictly true only when ε_* is constant, independent of n, for example, for infinite Peclet number or for $\varepsilon = 0$. Otherwise, Eq. (33) is an approximation because a complete orthogonal set is not guaranteed. As given by Eq. (30), 52 eigenfunctions are substituted into Eq. (33) for the calculations of the scalar variables; this gives a decent approximation to the infinite sum.

The values of c_n will be determined from the inflow conditions. Note that the flame will lie along the surface where the right side of Eq. (33) equals $Y_{Fs}/[\upsilon Y_{O\infty} + Y_{Fs}]$. From Eqs. (10) and (12), it follows that

$$\begin{aligned}(h - h_\infty)/Q = {} & [1 - (L_{\text{eff}}/Q)/(1 - Y_{Fs})](Y_{O\infty} - Y_O) \\ & + [(L_{\text{eff}}/Q)/(1 - Y_{Fs})](Y_{F\infty} - Y_F)\end{aligned} \tag{34}$$

Here, the subscript ∞ implies prescribed inflow conditions at $\tilde{x} = 0$. Equation (34) together with the phase-equilibrium law allows the determination of the temperature and the fuel vapor mass fraction at the liquid/gas interface without solving the gas flowfield first. Equation (34) includes the effect of Stefan convection at the interface in an exact fashion; however, Stefan convection in the partial differential equations governing the gas-phase behavior will be introduced in an iterative manner. That is, in this section, the Stefan convection has been neglected in Eq. (27). Its effect will be treated as a perturbation to the solution in Sec. VIII.

On the fuel side of the diffusion flame, $Y_O = 0$, whereas, on the oxidizer side, $Y_F = 0$; thus, the values of Y_F and Y_O are directly determined from Eq. (33). Equations (33) and (34) also apply for the case where some fuel vapor is combined with the inflowing oxidizer in a lean mixture. Then, a premixed flame exists upstream of the diffusion flame. Analysis of the premixed flame structure and propagation speed is necessary to resolve that phenomenon; a dependence on the chemical kinetic rate will occur. We will not consider that case here, so that $Y_{F\infty} = 0$ may be taken in Equation (34).

Classical Sturm-Liouville theory (see Refs. 28 and 29) yields that the coefficients

$$c_n = \int_0^{R_1/R} \left(\tilde{r} - \varepsilon_*^2\tilde{r}^3\right)\alpha(\tilde{r},0)\Theta_n(\tilde{r})\,\mathrm{d}\tilde{r} \Bigg/ \int_0^{R_1/R} \left(\tilde{r} - \varepsilon_*^2\tilde{r}^3\right)\Theta_n^2(\tilde{r})\,\mathrm{d}\tilde{r} \tag{35}$$

with $\alpha(\tilde{r}, 0) = 1$. Here, we will only consider the case where inlet condition $\alpha(\tilde{r}, 0)$ is uniform over the cross-sectional area of the inlet so that α may be taken outside of the integral in Eq. (35).

The eigenfunction-expansion analysis here is rigorous in the two limits where the Sturm–Liouville problem has been created. In the limit of infinite Peclet number, the axial heat conduction disappears and $\varepsilon_* = \varepsilon$. Previous investigators of the Graetz problem have reported that $Pe > 50$ (based on diameter) is sufficient to neglect axial heat conduction. In the other limit, the parabolic velocity profile is replaced by a plug-flow profile. Then, with $\varepsilon_* = 0$ as noted before,

$$\Theta_n = J_0(\lambda_n\tilde{r}) \tag{36a}$$

Furthermore, in that case,

$$c_n = 2/(\lambda_n R_i/R)J_1(\lambda_n R_i/R) \tag{36b}$$

where J_1 is the Bessel function of the first kind and first order. The eigenvalues λ_n are determined by $J_0(\lambda_n R_i/R) = 0$. The signs of $J_1(\lambda_n R_i/R)$ and c_n will alternate as the integer index n increases.

For the case where $\varepsilon \neq 0$, the integrals in Eq. (35) can be readily evaluated with substitution of the series given by Eq. (30) and with use of the quadrature

$$\int x^q e^{-x}\,\mathrm{d}x = -e^{-x}(q!)\sum_{\ell=0}^{q}\frac{x^\ell}{\ell!}$$

where q is any positive integer or zero. Then we find that

$$c_n = 2\left\{\sum_{q=0}^{\infty}\left(\frac{-1}{\beta_n}\right)^q \frac{\Pi_{p=0}^{q-1}(1-2p\beta_n)}{q!}\left[\tilde{G}_n(q) - \frac{\beta_n^2(q+1)}{\beta_n(1+\beta_n)} \times \tilde{G}_n(q+1)\right] \Bigg/ \sum_{q=0}^{\infty} F_n(q)\frac{q!}{(\beta_n/2)^q}\left[G_n(q) - \frac{\beta_n^2(q+1)}{2\beta_n(1+\beta_n)} \times G_n(q+1)\right]\right\} \tag{37a}$$

Furthermore, we have the definitions

$$F_n(q) \equiv \sum_{m=0}^{q} a_{2m}a_{2(q-m)} \tag{37b}$$

$$G_n(q) \equiv 1 - \exp\left(-\frac{\beta_n\gamma_n}{2}\right)\sum_{\ell=0}^{q}\left(\frac{\beta_n\gamma_n}{2}\right)^\ell\frac{1}{\ell!} \tag{37c}$$

$$\tilde{G}(q) \equiv 1 - \exp\left(-\frac{\beta_n\gamma_n}{4}\right)\sum_{\ell=0}^{q}\left(\frac{\beta_n\gamma_n}{4}\right)^\ell\frac{1}{\ell!} \tag{37d}$$

and

$$\gamma_n \equiv \left[4\varepsilon^2(1+\beta_n)\big/\beta_n^2\right](R_i/R)^2 \tag{37e}$$

In the calculation of the coefficients c_n in Eq. (37a), the infinite limit on the summations are approximated through the finite limit $q_{\max}$. The functions $G(q)$ and $\tilde{G}(q)$ will decrease with increasing q and theoretically will go to zero rapidly enough to cause convergence of the outermost sums in the numerator and denominator of Eq. (37a). In a practical computation, they reach a minimum value of the order of 10^{-16} and oscillate with that order of magnitude for increasing q. Thus, the c_n values will appear converged for a range of $q_{\max}$ values but will begin to vary as $q_{\max}$ is increased above that range as a result of the numerical errors associated with values of $G(q)$ and $\tilde{G}(q)$ that become too large for larger q values. A larger value of the index n results in the converged range of $q_{\max}$ occurring at higher values. Consequently, care was taken in choosing the $q_{\max}$ value to obtain convergence without causing the numerical error resulting from too large a value.

The local nondimensional vaporization rate per unit area can be determined as a function of downstream position by using the combination of Eqs. (8a), with the neglect of Stefan convection, and solution (33). The result is

$$\frac{\dot{m}R}{\rho D} = -[\upsilon Y_{O\infty} + Y_{Fs}]\sum_{n=1}^{\infty} c_n\Theta_n'(\tilde{r}_i)\exp(-k_n\tilde{x}) \tag{38}$$

Furthermore, differentiation of Eq. (30a) followed by substitution into result (38) and use of (31) yields

$$\frac{\dot{m}R}{\rho D} = -\frac{2}{\tilde{r}_i}[\upsilon Y_{O\infty} + Y_{Fs}]\sum_{n=1}^{\infty}\left[c_n\exp(-k_n\tilde{x})\eta_i\exp\left(-\frac{\beta_n\eta_i^2}{4}\right) \times \sum_{m=1}^{\infty} m a_{2m}\eta_i^{2m-1}\right] \tag{39}$$

Integration of Eq. (39) over the axial coordinate and the circumference gives the total nondimensional vaporization rate over the liquid surface,

$$\frac{2\pi R_i}{\rho D}\int_o^{L/R}\dot{m}\,\mathrm{d}\tilde{x} = 4\pi[\upsilon Y_{O\infty} + Y_{Fs}]\sum_{n=1}^{\infty}\left\{\frac{c_n}{k_n}\left[\exp\left(-\frac{k_n L}{R}\right) - 1\right]\eta_i\exp\left(-\frac{\beta_n\eta_i^2}{4}\right)\sum_{m=1}^{\infty} m a_{2m}\eta_i^{2m-1}\right\} \tag{40}$$

In the plug-flow limit of $\varepsilon = 0$, use of Eqs. (36) together with Eq. (38) yields that

$$\frac{\dot{m}R}{\rho D} = \frac{2}{\tilde{r}_i}[\upsilon Y_{O\infty} + Y_{Fs}]\sum_{n=1}^{\infty}\exp(-k_n\tilde{x}) \tag{41a}$$

$$\frac{2\pi R_i}{\rho D}\int_o^{L/R}\dot{m}\,\mathrm{d}\tilde{x} = 4\pi[\upsilon Y_{O\infty} + Y_{Fs}]\sum_{n=1}^{\infty}\frac{1-\exp(-k_n L/R)}{k_n} \tag{41b}$$

The major effect of fuel choice on vaporization effect comes through the parameter $\upsilon Y_{O\infty} + Y_{Fs}$ in Eqs. (38–41). A very minor influence occurs for the case with parabolic-velocity profile through the liquid viscosity which affects β_n and k_n through Eqs. (25c), (30c), (32), and (33) and, thereby, has the small influence on the vaporization rates given by Eqs. (39) and (40). Later, we shall discuss the effects of higher-order hydrodynamics (swirl-induced radial velocity, Stefan flow, and gas expansion) on the vaporization rate.

Figure 1 shows solutions of Eqs. (33) and (35) for a $Pe = 500$ and for a base flow with parabolic axial-velocity profile, that is, $\varepsilon \neq 0$. The solution for the scalar α does not depend on the choice of fuel; however, the contour value designating the thin-flame contour does depend on the fuel and oxidizer and the liquid temperature. The dashed line shows the flame contour for the heptane film at a bulk temperature of 298 K vaporizing into the gas stream with air as the inflowing gas. The α value decreases with an increase in the value

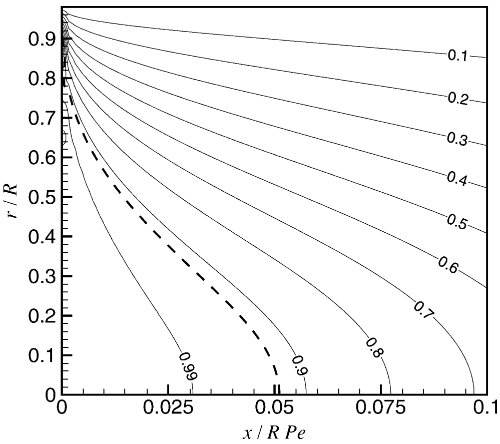

Fig. 1 Parabolic axial velocity profile α contours, $Pe = 500$: ---, heptane-flame contour.

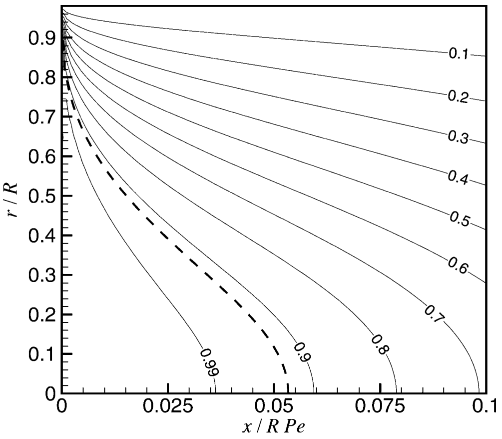

Fig. 2 Parabolic velocity profile α contours, $Pe = 1000$: ---, heptane-flame contour.

of the radial coordinate or of the axial coordinate. An increase of the Peclet number results in the relocation farther downstream of a contour curve representing a given value of the scalar. See Fig. 2 for the case where $Pe = 1000$. In fact, for Peclet number of 750 and above, the results essentially collapse to a function of $\tilde{r}$ and $\tilde{x}/Pe$, as noted earlier. More terms in the series solution of Eq. (33) are required for a converged solution as $\tilde{x}$ becomes smaller. Thus, we find some error in the contours for values of $\tilde{x}/Pe < 0.003$. For this small region, especially at higher $\tilde{r}$ values, 52 terms in the summation of Eq. (33) did not give convergence. These contours do not depend on the particular fuel that is used or the liquid interface temperature because the scalar in Eq. (33) goes to zero value at the liquid interface. The value of α at the flame position will depend on the choice of fuel and the liquid interface temperature. Figure 3 shows results for the plug-flow limit. Again, the results collapse to a function of $\tilde{r}$ and $\tilde{x}/Pe$ only for large Peclet number; the results for $Pe = 100$ and 500 are essentially superimposed. The results are qualitatively similar to the parabolic profile results, but for a given value of α, the contour line extends farther downstream. This can be expected because, for the same Peclet number, the plug flow has a greater average velocity than the parabolic flow.

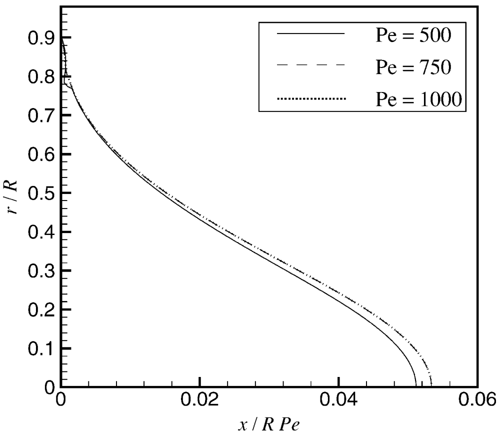

Fig. 3 Flame contour, parabolic velocity profile.

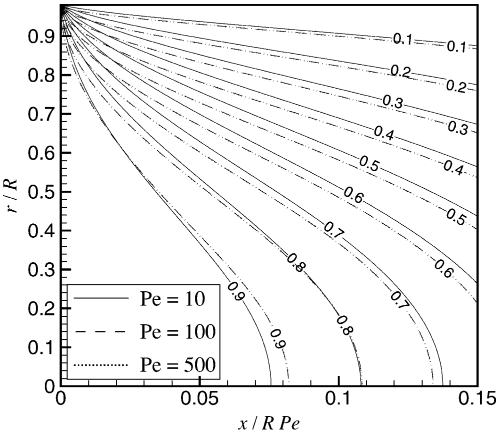

Fig. 4 Plug flow α contours.

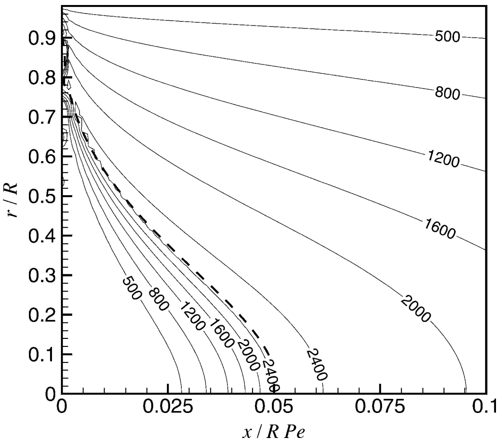

Fig. 5 Temperature contours (degrees Kelvin), parabolic axial velocity profile, $Pe = 500$, heptane.

The flame position for heptane fuel at a bulk temperature of 298 K is shown in Fig. 4 at three different Peclet numbers under the assumption of infinite chemical kinetic rate so that a flame of zero thickness results. As expected, the flame moves farther downstream with increasing Peclet number. At $Pe = 500$, the combustion is completed at approximately 12.5 diameters length as indicated by the flame collapsing to a point on the axis. The results for $Pe = 750$ and 1000 superimpose when plotted vs $\tilde{x}/Pe$. If relatively high mass flows and relatively short chamber lengths are desired, it is clear that the effective diffusivity must be increased (and the effective Peclet number must be reduced) through the generation of vortices or turbulence.

Temperature and mass fraction profiles for heptane with $Pe = 500$ are presented in Figs. 5 and 6. Peak temperature occurs at the flame with fuel vapor and oxidizer (air) each existing on only one side of the flame with both mass fractions decreasing with radial distance from the flame and going to zero values at the flame. For large Peclet number, the results for temperature and mass fraction will superimpose when plotted against $\tilde{x}/Pe$.

Figure 7 shows the changes in flame position due to change in the initial fuel temperature or change in fuel to methanol. Clearly, the heptane case leads to faster vaporization and shorter flame length,

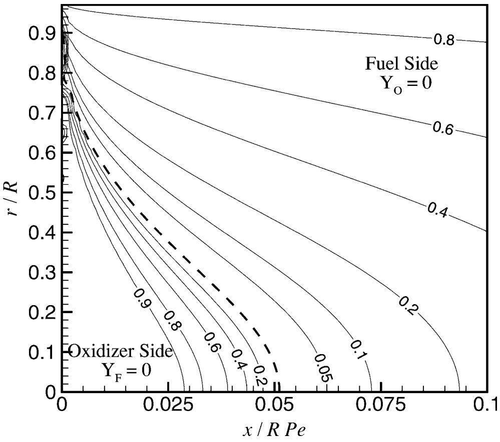

Fig. 6 Contours of oxidizer and fuel-vapor mass fractions, parabolic axial velocity profile, *Pe* = 500, heptane.

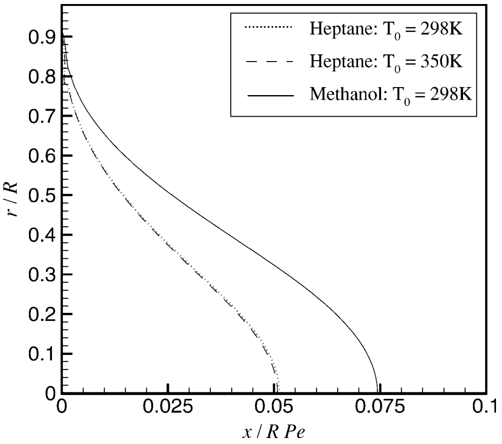

Fig. 7 Nondimensional flame position for change in fuel or initial fuel temperature, *Pe* = 500, parabolic axial velocity profile.

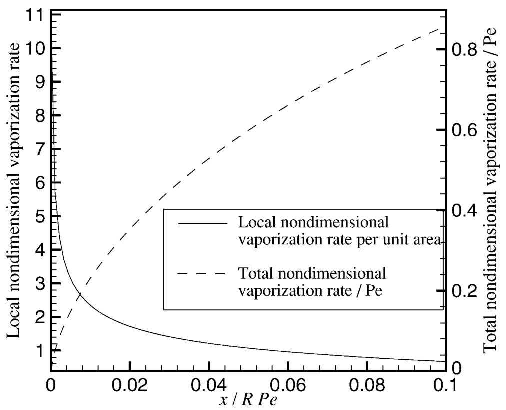

Fig. 8 Nondimensional (local and integrated) vaporization mass rates vs film length for heptane, *Pe* = 500, parabolic axial velocity profile.

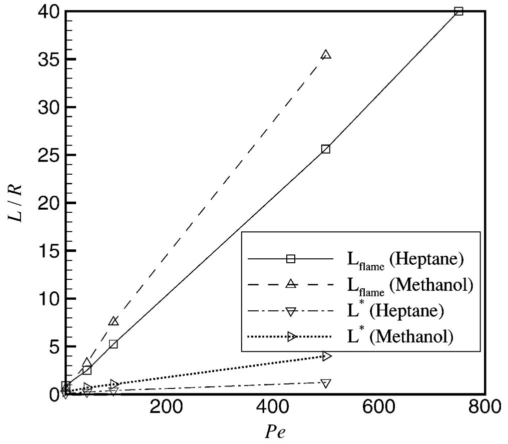

Fig. 9 Nondimensional flame length and stoichiometric liquid-film length vs Peclet number, parabolic axial velocity profile.

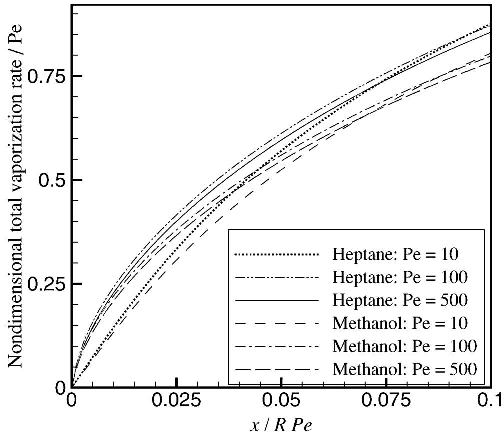

Fig. 10 Nondimensional total vaporization rates for methanol and heptane vs downstream position at various Peclet number values, parabolic axial velocity profile.

whereas a change in the initial fuel temperature has little effect. In Fig. 8, we show vaporization mass flux per unit area and integrated vaporization mass flux vs downstream distance for heptane with $Pe = 500$. The total, that is, integrated, vaporization rate is roughly proportional to Peclet number because the film length is determined to maintain stoichiometric proportions, whereas the air-inflow rate scales with Peclet number. Figure 9 shows an important implication of the integrated vaporization rate. L_{flame} is the downstream position at which combustion is completed, that is, it is the value of the x position where the flame crosses the axis of symmetry. As expected, it increases roughly linearly with increasing Peclet number at larger Peclet number values. Furthermore, a greater distance is required for the less volatile fuel, methanol, than for heptane. L^* is the fuel-film length required to vaporize at an integrated rate that matches, in stoichiometric proportion, the inflow of air. It is seen in Fig. 9 that $L^* < L_{\mathrm{flame}}$ for $Pe = 10$ or greater. A careful examination of the data indicates that the dependence of L^* on Peclet number is sublinear; that result is qualitatively in agreement with boundary-layer theory, which predicts a square-root dependence. The implication of the linear and sublinear dependencies is that a crossing of the curves will occur, but apparently, it happens for a very small Peclet number value. The result implies that, to protect the chamber wall for the full length needed to complete combustion, the fuel must be supplied in excess of stoichiometric mixtures. An alternative option not explored here is to mix the fuel with a less volatile inert liquid, for example, alcohol and water, to get the wall coverage for heat protection without exceeding stoichiometric proportions significantly, or the inert liquid could be applied to the chamber walls just downstream of the end of the fuel film. Also, the addition of turbulence or vorticity in the gas can create a larger value of the effective diffusivity. Qualitatively, this is similar to decreasing the value of Peclet number, implying that the increased transport rates will shorten the required lengths for completion of vaporization and combustion. As noted earlier, an error in the use of the eigenfunction expansion increases as Peclet number becomes smaller.

Figure 10 is an extension of the results of Fig. 8 for the integrated vaporization rate to other Peclet numbers and shows data for both heptane and methanol. Integrated vaporization rates increase with increasing Peclet number, and methanol vaporizes at a slightly lower rate than heptane. The longer required lengths for film vaporization and completion of combustion for methanol appear to be primarily caused by the greater amount of methanol-vapor mass flux than heptane-vapor mass flux needed for a given air mass flow to maintain a stoichiometric proportion.

Generally, at this time, only qualitative comparisons with experiments can readily be made. Currently, there are no experimental measurements of gas-phase and liquid-phase temperature and velocity and gas-phase concentrations inside a liquid-film combustor. There are some measurements[10,12,13] of wall temperatures and exit temperatures. The wall temperatures are below the liquid boiling point, in agreement with the theory, indicating that the liquid is insulating the wall. The exit-temperature measurements reinforce the clear visual observation that combustion of all of the fuel does not occur within the combustor; the flame is continued beyond the cylinder exit for the Peclet numbers tested. That is, for the higher values of Pe, $L^* < L_{\mathrm{flame}}$ as predicted by the calculations shown in Fig. 9. Some unpublished results indicate that, in certain flow rate ranges, overall flame length can decrease as air and fuel flow rates increase. It is likely that vorticity generation is increasing sufficiently with increasing flow rate so that the effective diffusivity increases and the effective Peclet number decreases, thereby decreasing flame length as indicated by Fig. 9.

The results indicate that the liquid-film combustion is feasible; although for this simple laminar flow, the required chamber length is an order of magnitude larger than the diameter. This indicates a need to impose swirl and/or vortex generation to increase transport rates and thereby reduce the required chamber length. In the next section, the effect of swirl imposed on the inflow is considered as a perturbation to the base flow. Similarly, perturbations to this base flow due to the Stefan velocity and the density variation are evaluated in a later section.

VI. Swirling Flow Perturbation

The tangential velocity component is described by Eq. (22). Consider that the tangential velocity can be represented in a separable form as

$$w_1(\tilde{r}, \tilde{x}) = u_c W_n(\tilde{r}) \exp(-k_n \tilde{x}) \tag{42}$$

where the nondimensional eigenvalue k_n differs from the values found in the scalar analysis and the Reynolds number Re is given by

$$Re \equiv \rho_0 u_c R / \mu_0 \tag{43}$$

Whereas the base axial flow is developed, the tangential velocity field is developing, and therefore, the Reynolds number Re value is important. Also, the variable ζ is defined so that

$$u_0 = u_c[1 - \zeta(\tilde{r})] \tag{44a}$$

Note that ζ is the nondimensional velocity defect $(u_c - u_0)/u_c = u_d/u_c$. Furthermore, for $0 \le \tilde{r} \le R_i/R$,

$$\zeta = \varepsilon^2 \tilde{r} \tag{44b}$$

and for $R_i/R \le \tilde{r} \le 1$,

$$\zeta = 1 - \left[\frac{1 - \tilde{r}^2}{1 - (1 - \mu_l/\mu_g)(R_i/R)^2}\right] \tag{44c}$$

Then, we can obtain the ordinary differential equation for W_n by substituting Eq. (42) into the nondimensional form of Eq. (22),

$$\frac{\mathrm{d}}{\mathrm{d}\tilde{r}}\left[\tilde{r}\frac{\mathrm{d}W_n}{\mathrm{d}\tilde{r}}\right] - \frac{W_n}{\tilde{r}} + \left[\frac{Re(1 - \zeta)}{\delta}k_n + k_n^2\right]\tilde{r}W_n = 0 \tag{45}$$

where δ is defined with unity value in the gas, whereas $\delta = \mu_l/\mu_g$ in the liquid.

Equation (45) does not meet the Sturm–Liouville form for two reasons. First, the appearance of k_n^2 in the coefficient destroys the standard form. (However, in the limit of large Reynolds number or in the limit of small ε, this is not significant.) Second, the discontinuity in the first derivative at the gas/liquid interface cannot be tolerated. This problem can be overcome by a transformation of the independent variable. For the axial flow, the shear stress is given by

$$\tau = \mu\frac{\partial u_0}{\partial r} = -\mu\frac{\partial u_d}{\partial r} \tag{46}$$

From Eq. (21), τ is found to be linear in the radial position and proportional to the pressure gradient. Most important, it is continuous across the liquid/gas interface even though the velocity gradient is discontinuous. If we transform the independent variable from r to u_d for the case of nonzero ε value, it follows that

$$\frac{\mathrm{d}W_n}{\mathrm{d}r} = -\frac{\tau}{\mu}\frac{\mathrm{d}W_n}{\mathrm{d}u_d} = \left(-\frac{1}{2\mu}\frac{\mathrm{d}p_0}{\mathrm{d}x}\right)\frac{\mathrm{d}W_n}{\mathrm{d}u_d} \tag{47a}$$

The first derivative with respect to the velocity defect is continuous at the interface; therefore, a Sturm–Liouville form can be created.

In nondimensional terms, ζ becomes the independent variable (rather than $\tilde{r}$) yielding

$$\frac{\mathrm{d}W_n}{\mathrm{d}\tilde{r}} = \frac{\mathrm{d}\zeta}{\mathrm{d}\tilde{r}}\frac{\mathrm{d}W_n}{\mathrm{d}\zeta} = \frac{2\varepsilon^2}{\delta}\tilde{r}\frac{\mathrm{d}W_n}{\mathrm{d}\zeta} \tag{47b}$$

Equation (45) can now be written as

$$\frac{\mathrm{d}}{\mathrm{d}\zeta}\left(\tilde{r}^2\frac{\mathrm{d}W_n}{\mathrm{d}\zeta}\right) + \frac{\delta}{(2\varepsilon^2)^2}\left[(1 - \zeta)k_n Re + \delta k_n^2 - \frac{\delta}{\tilde{r}^2}\right]W_n = 0 \tag{48}$$

The discontinuity in δ will result in a discontinuity of the second derivative at the liquid/gas interface. Because W_n and its first derivative are continuous, the Sturm–Liouville form is still obtained in the limit of infinite Reynolds number.

Equation (48) guides us in the choice of the proper weighting factors in integrals to determine coefficients in eigenfunction expansions. We are still allowed to use either Eq. (45) or (48) in generating the eigenfunctions. We choose the former here. First, we solve for W_n in the region $0 \le \tilde{r} \le R_i/R$ where $\delta = 1$. It is convenient to set

$$\bar{r} = \sqrt{2\varepsilon}(k_n Re)^{\frac{1}{4}}\tilde{r}, \qquad W_n = \phi_n \exp(-\bar{r}^2/4)$$

$$\lambda_n = \left(\sqrt{k_n Re}/2\varepsilon\right)(1 + k_n/Re) \tag{49}$$

Then, Eq. (45) can be written for $0 \le \tilde{r} \le R_i/R$ or $0 \le \bar{r} \le \sqrt{}2\varepsilon\,(k_n Re)^{1/4} R_i/R$ and n equal to any positive integer as

$$\frac{\mathrm{d}^2\phi_n}{\mathrm{d}\bar{r}^2} + \left(\frac{1}{\bar{r}} - \bar{r}\right)\frac{\mathrm{d}\phi_n}{\mathrm{d}\bar{r}} - \left(1 + \frac{1}{\bar{r}^2}\right)\phi_n + \lambda_n\phi_n = 0 \tag{50}$$

where $\bar{r} = 0$ is a regular singular point. Casting away the solution with a logarithmic singularity, we obtain for the gas region

$$\phi_n = \bar{r} + \sum_{m=1}^{\infty}\frac{\pi_{p=1}^{m}[(2p - \lambda_n)/4]}{m!(m + 1)!}\bar{r}^{2m+1} \tag{51a}$$

$$W_n = \frac{(k_n Re)^{\frac{1}{4}}}{\sqrt{8\varepsilon}}\left[\bar{r} + \sum_{m=1}^{\infty}\frac{\pi_{p=1}^{m}[(2p - \lambda_n)/4]}{m!(m + 1)!}\bar{r}^{2m+1}\right]\exp\left(-\frac{\bar{r}^2}{4}\right) \tag{51b}$$

The constant $(k_n Re)^{\frac{1}{4}}/\sqrt{8\varepsilon}$ is designed to make W_n equal to the Bessel function $J_1[\sqrt{}(k_n Re)\tilde{r}]$ in the limit as ε tends to zero. Now, let us consider the liquid region. For that domain, it is convenient to seek a series solution in powers of $\xi = 1 - \tilde{r}^2$. Note that

$$\zeta = 1 - (\varepsilon^2/\delta)\xi$$

Equation (48) now becomes

$$\frac{\mathrm{d}}{\mathrm{d}\xi}\left((1 - \xi)\frac{\mathrm{d}W_n}{\mathrm{d}\xi}\right) - \frac{W_n}{4(1 - \xi)} + \Omega_n\left[\xi + \Omega_n\left(\frac{\delta}{Re\varepsilon}\right)^2\right]W_n = 0 \tag{52}$$

where

$$\Omega_n \equiv k_n Re(\varepsilon/2\delta)^2$$

A boundary condition at the wall, $r = R$ ($\tilde{r} = 1$ or $\xi = 0$), is that $W_n = 0$ due to the no-slip condition. Here $\xi = 0$ is an ordinary point, and a two Taylor series solution can be constructed for W_n in powers of ξ. Because of the no-slip condition, the constant before one of the solutions is set to zero and the other solution becomes the general solution. In particular,

$$W_n = \bar{c}_n \sum_{m-1}^{\infty} b_m \xi^m = \bar{c}_n \left[\xi + \frac{1}{2}\xi^2 + \frac{1-\alpha_n}{3}\xi^3 + \left(\frac{1}{4} - \frac{\alpha_n}{3} - \frac{\beta}{12}\right)\xi^4 + - - - \right] \tag{53}$$

where

$$\alpha_n \equiv \left(k_n^2 - 1\right)\big/8, \qquad \beta \equiv [Re(\varepsilon/\delta)^2 - 1]/4$$

The recursive relation for b_m is

$$b_{m+2} = \frac{m+1}{m+2} b_{m+1} - \frac{2\alpha_n b_m}{(m+2)(m+1)} - \frac{\beta b_{m-1}}{(m+2)(m+1)} + \frac{\sum_{p=0}^{m-2} b_p}{4(m+2)(m+1)} \tag{54}$$

Equations (51) and (53) can be used to match the velocity and shear stress across the interface. That is, W_n and $\mu \mathrm{d}W_n/\mathrm{d}\tilde{r}$ are continuous across the interface. Two relations are yielded that determine k_n and $\bar{c}_n$ values. For thin liquid films, the relations determining k_n can be simplified.

From Eq. (53), it follows that, for small ξ values within the liquid,

$$\frac{1}{W_n}\frac{\mathrm{d}W_n}{\mathrm{d}\tilde{r}} = -\frac{2\tilde{r}}{\xi} + \mathcal{O}(1)$$

Thus, a linear approximation relating W_n and $\mathrm{d}W_n/\mathrm{d}\tilde{r}$ within the gas at R_i can be obtained and used as a boundary condition on Eq. (45). That is,

$$\left.\frac{\mathrm{d}W_n}{\mathrm{d}\tilde{r}}\right)_{\mathrm{gas},R_i/R} = -\frac{2\mu_\ell}{\mu_g}\frac{R_i R}{R^2 - R_i^2} W_n\left(\frac{R_i}{R}\right) \tag{55}$$

Note that the value of $W_n$in Eq. (55) will depend on the film thickness; W_n goes to zero as $R - R_i$ goes to zero. Because the thickness varies with downstream position, an average value must be used in Eq. (55) to allow separation of variables. Substitution of Eq. (51) into Eq. (55) yields a relationship that determines the eigenvalues k_n (or λ_n),

$$1 + \frac{1}{2}\frac{\mu_g}{\mu_\ell}\frac{R^2 - R_i^2}{R_i^2} + \frac{1}{4}\sum_{m=1}^{\infty}\left(\left\{\frac{\mu_g}{\mu_\ell}\frac{\left(R^2 - R_i^2\right)}{R_1^2}\frac{[m - \lambda_n - (\lambda_n/2m)]}{(m-1)!} + \frac{2m - \lambda_n}{m!}\right\}\frac{\pi_{p=1}^{m-1}[(2p - \lambda_n)/4]}{(m+1)!}\bar{r}_i^{2m}\right) = 0 \tag{56}$$

Note that, when $m = 1$,

$$\pi_{p=1}^{0}[(2p - \lambda_n)/4] \equiv 1$$

We can now obtain a general solution of the form

$$\frac{w_1}{u_c} = \sum_{n=0}^{\infty} c_n W_n \exp(-k_n \tilde{x}) \tag{57a}$$

where c_n can be determined from the profile of w_1/u_c for inflow at $\tilde{x} = 0$. That is,

$$c_n = \frac{\int_0^{R_i/R}\left[(Re + k_n)\tilde{r} - Re\varepsilon^2\tilde{r}^3\right] W_n (w_1/u_c)\big)_{\tilde{x}=0}\,\mathrm{d}\tilde{r}}{\int_0^{R_i/R}\left[(Re + k_n)\tilde{r} - Re\varepsilon^2\tilde{r}^3\right] W_n^2\,\mathrm{d}\tilde{r}} \tag{57b}$$

Note that Eqs. (57a) and (57b) are only exact in the limit where $Re \to \infty$ and $Re + k_n \to Re$ so that the eigenfunction expansion becomes valid. Otherwise, they only give an approximation.

In the limit $Re \to \infty$, Eq. (45) and its boundary condition provided by Eq. (55) together with Eq. (49) indicate that W_n becomes independent of Reynolds number and k_n becomes inversely proportional to Reynolds number. Then, Eq. (42) can show that the $\tilde{x}$ and Reynolds number dependencies appear only through the variable $\tilde{x}/Re$. Consider now, as one example, the inflow profile

$$\left.\frac{w_1}{u_c}\right)_{\tilde{x}=0} = \Omega(\tilde{r} - a\tilde{r}^3) \tag{58a}$$

which is zero at $\tilde{r} = 0$, increases with $\tilde{r}$ until a maximum is reached, and then decreases with further increase of $\tilde{r}$. Equation (58a) is made to satisfy the interface condition given by Eq. (55) so that

$$a = \frac{1 - (R_i/R)^2 + 2(\mu_\ell/\mu_g)(R_i/R)^2}{3(R_i/R)^2 - 3(R_i/R)^4 + 2(\mu_\ell/\mu_g)(R_i/R)^4} \tag{58b}$$

We shall take $\Omega = 1$ in Eq. (58). For this inflow profile, it can be shown that

$$c_n = \left(\frac{2\lambda_n}{\sqrt{k_n Re}} I_{3,n} - \frac{a\lambda_n}{\varepsilon k_n Re} I_{4,n} - \frac{1}{2\sqrt{k_n Re}} I_{4,n} + \frac{a}{4\varepsilon k_n Re} I_{5,n}\right)\Bigg/ \left(\lambda_n I_{1,n} - \frac{1}{4} I_{2,n}\right) \tag{59}$$

where

$$I_{1,n} = \sum_{q=0}^{\infty} F_{1,n}(q) G_{1,n}(q+1) H_{1,n}(q+1)$$

$$I_{2,n} = \sum_{q=0}^{\infty} F_{1,n}(q) G_{1,n}(q+2) H_{1,n}(q+2)$$

$$F_{1,n}(q) \equiv \sum_{m=0}^{q} a_m a_{q-m}$$

$$a_0 \equiv 1; \qquad a_m \equiv \frac{\pi_{p=1}^{m}[(2p - \lambda_n)/4]}{m!(m+1)!}$$

$$G_{1,n}(q) \equiv 1 - \exp\left(-\frac{\bar{r}_i^2}{2}\right)\sum_{\ell=0}^{q}\frac{\bar{r}_i^{2\ell}/2^\ell}{\ell!}$$

$$H_{1,n}(q) \equiv 2^q(q!)$$

$$I_{3,n} \equiv 8\sum_{q=0}^{\infty}\tilde{F}_{1,n}(q)\tilde{G}_{1,n}(q+1)$$

$$I_{4,n} \equiv 32\sum_{q=0}^{\infty}[q+2]\tilde{F}_{1,n}(q)\tilde{G}_{1,n}(q+2)$$

$$I_{5,n} \equiv 128\sum_{q=0}^{\infty}[q+2][q+3]\tilde{F}_{1,n}(q)\tilde{G}_{1,n}(q+3)$$

$$\tilde{F}_{1,n}(q) \equiv \frac{\pi_{p=1}^{q}(2p - \lambda_n)}{q!}$$

When $q = 0$, $\tilde{F}_{1,n} = 1$,

$$\tilde{G}_{1,n}(q) \equiv 1 - \exp\left(-\frac{\bar{r}_i^2}{4}\right)\sum_{\ell=0}^{q}\frac{\bar{r}_i^{2\ell}/4^\ell}{\ell!}$$

Equations (49) and (59) show that c_n becomes independent of Reynolds number for large values of Reynolds number.

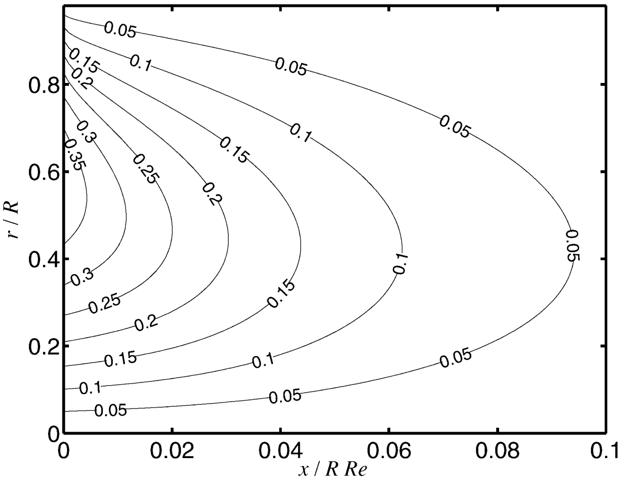

Fig. 11 Contours of nondimensional tangential velocity component (normalized by axial centerline velocity component) for *Re* = 1000, parabolic axial velocity profile.

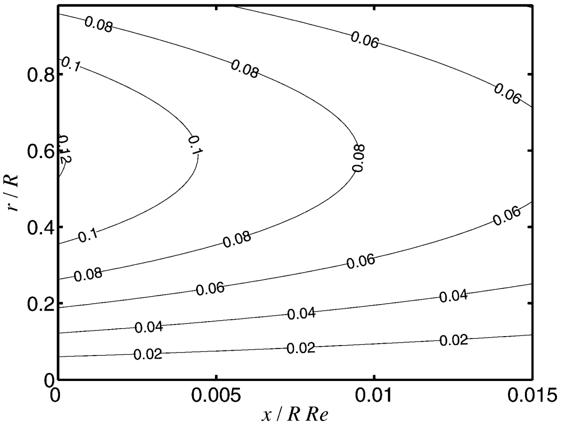

Fig. 12 Contours of normalized radial pressure gradient for *Re* = 1000, parabolic axial velocity profile.

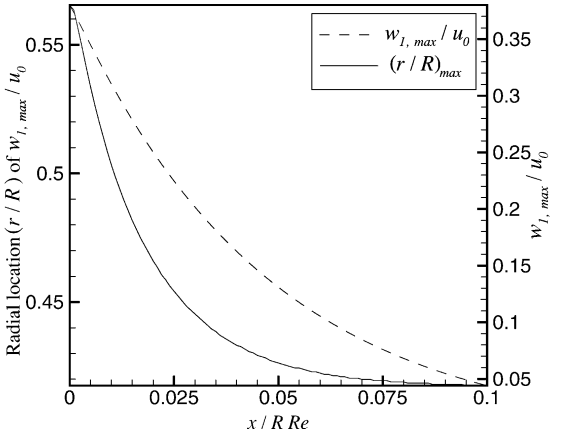

Fig. 13 Maximum value of nondimensional tangential velocity in radial profile and radial location of maximum value vs $\tilde{x}$/*Re* for *Re* = 500, 750, and 1000, parabolic axial velocity profile.

Figure 11 presents the nondimensional tangential velocity component, whereas Fig. 12 presents the nondimensional radial pressure gradient that results from the imposed swirl. Figure 11 shows that the magnitude of the tangential component decays with downstream distance, although the radial profile is roughly similar to the imposed profile at $\tilde{x} = 0$. The value of the maximum in the radial profile decreases substantially with increasing downstream distance, whereas the radial location of the maximum value changes very slightly. There are also slight decreases in the tangential velocity values at the liquid interface and at the centerline with increasing downstream distance. In Fig. 12, we find that the radial pressure gradient has the same qualitative features as the tangential velocity, although quantitative differences do exist resulting in the inducement of a radial velocity component as will be discussed in the next section. The peak in the radial pressure gradient occurs at a slightly larger radius, and the decrease in its value at the liquid interface with increasing downstream distance is faster. The radial pressure gradient is always positive so that pressure increases everywhere monotonically with radius. The maximum values of tangential velocity and of radial pressure gradient decay with increasing downstream coordinate value. The location of the maximum tangential velocity moves toward the symmetry axis with downstream distance, whereas the radial location of the pressure-gradient maximum varies much less. The rate of decay with downstream distance for both the tangential velocity gradient and the radial pressure gradient will decrease as the Reynolds number *Re* becomes larger. Again, for very large Reynolds number, the primary dependencies on both $\tilde{x}$ and Reynolds number appear through the variable $\tilde{x}/Re$. At a given value of $\tilde{x}/Re$, the radial profile becomes independent of Reynolds number for large values of *Re*. Figure 13 shows the maximum tangential velocity value in the radial profile and the radial location of that maximum value vs $\tilde{x}/Re$ for various values of Reynolds number. The curves for the maximum value fall together when plotted vs the x location normalized by the Reynolds number. The radial location of the maximum also has the $\tilde{x}/Re$ dependence, for large Reynolds number.

In the limit where $\varepsilon = 0$ (plug flow) with the neglect of the streamwise derivative of viscous stress, Eq. (45) becomes a Bessel equation. Then, Eq. (51) with the constraint of finite magnitude yields the solution $W_n(\tilde{r}) = J_1[\sqrt{(k_n Re)}\tilde{r}]$. Equation (55) will be applied to determine the eigenvalues for the Bessel equation.

VII. Swirl-Induced Hydrodynamics

Until this point, the analysis has emphasized the base flow with parabolic velocity profile, and plug flow has been considered as a limiting case. To avoid some more complex algebra and calculus, certain simplifications are made for the analysis in these remaining sections. In particular, $\varepsilon = 0$ (plug flow) is assumed, and so u_0 is a constant. The dimensional equations governing u_1, v_1, and ρ_1 with constant viscosity are

$$\rho_0 \frac{\partial u_1}{\partial x} + \frac{\rho_0}{r}\frac{\partial}{\partial r}(v_1 r) = -u_0 \frac{\partial \rho_1}{\partial x} \tag{60a}$$

$$\rho_0 u_0 \frac{\partial u_1}{\partial x} + \frac{\partial p_1}{\partial x} = \frac{\mu_0}{r}\frac{\partial}{\partial r}\left(r\frac{\partial u_1}{\partial r}\right) + \mu_0 \frac{\partial^2 u_1}{\partial x^2} - \frac{1}{3}\frac{\mu_0 u_0}{\rho_0}\frac{\partial^2 \rho_1}{\partial x^2} \tag{60b}$$

$$\rho_0 u_0 \frac{\partial v_1}{\partial x} + \frac{\partial p_1}{\partial r} - \rho_0 \frac{w_1^2}{r} = \frac{\mu_0}{r}\frac{\partial}{\partial r}\left(r\frac{\partial v_1}{\partial r}\right) - \frac{\mu_0 v_1}{r^2} + \mu_0 \frac{\partial^2 v_1}{\partial x^2} + \frac{2\mu_0}{3\rho_0}\left[\frac{\partial(u_0)}{\partial r}\frac{\partial \rho_1}{\partial x} + u_0 \frac{\partial^2 \rho_1}{\partial r \partial x}\right] \tag{60c}$$

and p_1 and ρ_1 will be connected through an equation of state. However, density variation occurs primarily because of temperature variation. For the moment, density perturbations will not be considered, that is, $\rho_1 = 0$; that linear effect will be added in the next section. Note that the term $(-\rho_0 w_1^2/r)$ in Eq. (60c) is actually a higher-order term. It is kept in Eq. (60) because in practice the centrifugal effect might be the dominant factor in determining the radial pressure gradient. With w_1 given via the solution method indicated in the preceding section, the problem stated by Eq. (60) remains linear.

A radial velocity will be created by both the Stefan flow and the imposed swirl. Let us first consider the velocity and pressure perturbation due to the imposed swirl. The imposed swirl velocity at $x = 0$ is simply taken as $w_1 = cu_0 J_1(\lambda_1 \tilde{r})$, where $\lambda_1 \tilde{r}_i$ is the lowest value satisfying Eq. (55) and c is a given constant. The same nondimensional scheme from earlier sections is used. Separation can be assumed for these linear equations so that

$$u_1/u_0 = U(\tilde{r})\exp(-\lambda\tilde{x}) \tag{61a}$$

$$v_1/u_0 = V(\tilde{r})\exp(-\lambda\tilde{x}) \tag{61b}$$

$$p_1\big/\rho_0 u_0^2 = P(\tilde{r})\exp(-\lambda\tilde{x}) \tag{61c}$$

Note that

$$w_1^2\big/u_0^2 = c^2 J_1^2(\lambda_1\tilde{r})\exp(-2k_1\tilde{x}) \tag{61d}$$

with $k_1 = \lambda_1^2/Re$.

We will consider first the values of u_1, v_1, and p_1 caused by the swirl velocity. We will add the particular and homogeneous solutions for the linear problem given by Eq. (60). Equations (60a–60c) become after separation

$$-\lambda U + \frac{1}{\tilde{r}}\frac{\mathrm{d}}{\mathrm{d}\tilde{r}}(V\tilde{r}) = 0 \tag{62a}$$

$$-\lambda U - \lambda P - \frac{1}{Re}\frac{1}{\tilde{r}}\frac{\mathrm{d}}{\mathrm{d}\tilde{r}}\left(\tilde{r}\frac{\mathrm{d}U}{\mathrm{d}\tilde{r}}\right) - \frac{\lambda^2}{Re}U = 0 \tag{62b}$$

$$-\lambda V + \frac{\mathrm{d}P}{\mathrm{d}\tilde{r}} - \frac{1}{Re}\left[\frac{1}{\tilde{r}}\frac{\mathrm{d}}{\mathrm{d}\tilde{r}}\left(\tilde{r}\frac{\mathrm{d}V}{\mathrm{d}\tilde{r}}\right) - \frac{V}{\tilde{r}^2}\right] - \frac{\lambda^2}{Re}V = \frac{c^2 J_1^2(\lambda_1\tilde{r})}{\tilde{r}} \tag{62c}$$

When exponents are matched, $\lambda = 2k_1$ for the particular solution, whereas it remains to be determined for the homogeneous solutions. Also, the right side of Eq. (62c) becomes zero for the homogeneous solution. First, we will seek the particular solution.

Before solution of Eqs. (62a–62c), certain behavior can be noted by inspection for large Reynolds number. From Eq. (62b), we see that λ must be of the order of $1/Re$, which is small compared to unity. Then, the last terms on the left sides of Eqs. (62b) and (62c) are negligible compared to other terms. More importantly, the radial pressure gradient and centrifugal acceleration terms in Eq. (62c) balance each other to lowest order. Note that the variations of w_1 and p_1 in the $\tilde{x}$ direction are negligible in this high Reynolds number limit.

In solving the system of equations, we will neglect those stress terms of order (λ^2/Re) that originated from the second derivatives in the $\tilde{x}$ direction. Equations (62a) and (62b) can be combined to eliminate U, giving P in terms of V and its first three derivatives. Substitution for the derivative of P in Eq. (62c) yields a fourth-order system for V,

$$\frac{\mathrm{d}^2 V}{\mathrm{d}\tilde{r}^2} + \frac{1}{\tilde{r}}\frac{\mathrm{d}V}{\mathrm{d}\tilde{r}} - \frac{V}{\tilde{r}^2} = \zeta \tag{63a}$$

$$\frac{\mathrm{d}^2 \zeta}{\mathrm{d}\tilde{r}^2} + \frac{1}{\tilde{r}}\frac{\mathrm{d}\zeta}{\mathrm{d}\tilde{r}} - \frac{\zeta}{\tilde{r}^2} + \lambda^2\left(1 + \frac{Re}{\lambda}\right)\zeta + Re\lambda^3 V = -Re\lambda^2 c^2\frac{J_1^2(\lambda_1\tilde{r})}{\tilde{r}} \tag{63b}$$

where ζ is a conveniently defined variable with no particular physical interpretation.

Certain boundary conditions can be applied on the fourth-order system. We expect that $V = 0$ at $\tilde{r} = 0$. From the symmetry of U at $\tilde{r} = 0$, it follows from Eqs. (62a) and (63a) that $V''(0) = (2/3)\zeta(0) = 0$. At $\tilde{r}_i = R_i/R$, we take $V(\tilde{r}_i) = 0$ and, when the no-slip condition at the interface for this plug-flow case is replaced with a zero-shear-stress condition, $U'(\tilde{r}_i) = 0$. These four boundary conditions on V and its derivatives are sufficient to solve the system of equations given by Eqs. (63a) and (63b).

We can find a solution to Eq. (63) of the form

$$V = \sum_{m=0}^{\infty} b_m \tilde{r}^{2m+1} \tag{64a}$$

Substitution into Eq. (62a) yields that

$$U = \frac{2}{\lambda}\sum_{m=0}^{\infty}(1+m)b_m\tilde{r}^{2m} = \frac{1}{k_1}\sum_{m=0}^{\infty}(1+m)b_m\tilde{r}^{2m} \tag{64b}$$

Substitution of Eq. (64a) into Eq. (63) gives the recursive relation that governs b_m

$$b_{m+2} = -\frac{\lambda^2}{4}\frac{1 + Re/\lambda}{(m+2)(m+3)}b_{m+1} - \frac{Re\lambda^3}{16(m+1)(m+2)^2(m+3)} \times b_m - \frac{Re\lambda^2 c^2 \lambda_1}{16(m+1)(m+2)^2(m+3)}A_m\lambda_1^{2m+1} \tag{64c}$$

where the manipulation with the Bessel function gives

$$A_m = \frac{1}{4}\left(-\frac{1}{4}\right)^m \sum_{q=0}^{m}\frac{1}{q!(q+1)!(m-q)!(m-q+1)!} \tag{64d}$$

Equation (64a) satisfies the two boundary conditions at $\tilde{r} = 0$. Equation (64c) gives b_2, b_3, b_4, etc., in terms of b_0 and b_1. Those first two coefficients can be determined by applying the boundary conditions at $\tilde{r}_i$, which give

$$\sum_{m=0}^{\infty} b_m\tilde{r}_i^{2m+1} = 0, \qquad \sum_{m=0}^{\infty} m(1+m)b_m\tilde{r}_i^{2m} = 0 \tag{64e}$$

The coefficients b_m for $m = 0, 1, \ldots, N$ can be determined with sufficient accuracy for large N values by truncating the summations in Eqs. (64e) after the first $N + 1$ terms. Then Eqs. (64c–64e,) yield a linear algebraic system for the coefficients.

Equation (64c) can be taken to the infinite Reynolds number Re limit, noting $\lambda = 2k_1 = O(Re^{-1})$, so that

$$b_{m+2} = -\frac{\lambda_1^2 c}{2(m+2)(m+3)}b_{m+1} \tag{65}$$

Now, Eq. (65) allows the determination of coefficients $b_{1,}b_2$, b_3, b_4, etc., in terms of b_0, whereas the first constraint of Eq. (64e) allows the determination of b_0. Thus, some error is allowed with this solution. This can be viewed as a good approximation at high Reynolds number for a core flow with poor resolution of the gas boundary layer near the liquid film. Note that, in this inviscid limit, the coefficients b_m do not depend on the tangential component of velocity. As a consequence, the first Eq. (64e) combined with Eq. (65) yield that $b_m = 0$ for all values of m. The interpretation of this high Reynolds number plug-flow particular solution is that the radial pressure gradient term equals the centrifugal acceleration term with the radial velocity and axial velocity perturbations being zero. If the radial velocity and axial velocity perturbations are zero at inflow, this particular solution gives the total solution and the velocity perturbations due to swirl will be zero throughout the flow. There would not be any pressure gradient in the axial direction. If the inflow conditions are nonzero, the homogeneous solution to Eqs. (62a–62c) will present the velocity field. If the Reynolds number is not taken to the limit, Eq. (64c) is used rather than Eq. (65). Then, the swirl-induced centrifugal acceleration is not immediately balanced by the pressure gradient, and b_m will not be zero for values of the integer index m.

To satisfy specific inflow conditions, a homogeneous (nonswirling) solution of Eqs. (61) and (62) must be added to the earlier described solution. Now, consider the homogeneous solution for Eqs. (62a–62c). The homogeneous solution of Eqs. (62), or equivalently Eqs. (63a) and (63b), is fortuitously the same solution found in the inviscid (infinite Reynolds number) limit,

$$U(\tilde{r}) = J_0(\bar{\lambda}_n \tilde{r}), \qquad V(\tilde{r}) = J_1(\bar{\lambda}_n \tilde{r}) \tag{66}$$

that is, the same velocity solution holds for the inviscid and viscous (with slip at the liquid interface) solutions in this constant density and viscosity problem. Solutions (66) satisfy the homogeneous boundary conditions at $\tilde{r} = 0$. $V(\tilde{r}_i) = 0$ is obtained by choosing $\bar{\lambda}_n \tilde{r}_i$ to be a root of J_1. Of course, this simple form of the homogeneous solution to Eqs. (62) will not satisfy the no-slip boundary condition on the axial component of velocity.

Here, we will consider that the radial velocity at inflow is zero. Radial acceleration of the flow due to the swirl begins immediately at inflow. It follows from the combination of the homogeneous solution with the swirl-induced solution that

$$\frac{u_{1\mathrm{sw}}}{u_0} = \frac{1}{k_1} \exp(-2k_1 \tilde{x}) \sum_{m=0}^{\infty} (1+m) b_m \tilde{r}^{2m} - \sum_{n=0}^{\infty} \bar{c}_n J_0(\bar{\lambda}_n \tilde{r}) \exp(-\bar{\lambda}_n \tilde{x}) \tag{67a}$$

$$\frac{v_{1\mathrm{sw}}}{u_0} = \exp(-2k_1 \tilde{x}) \sum_{m=0}^{\infty} b_m \tilde{r}^{2m+1} - \sum_{n=0}^{\infty} \bar{c}_n J_1(\bar{\lambda}_n \tilde{r}) \exp(-\bar{\lambda}_n \tilde{x}) \tag{67b}$$

The coefficients $\bar{c}_n$ are chosen to give $v_{1\mathrm{sw}} = 0$ at $\tilde{x} = 0$. Namely,

$$\bar{c}_n = \frac{2}{\tilde{r}_i^2 J_2^2(\bar{\lambda}_n \tilde{r}_i)} \int_0^{\tilde{r}_i} \tilde{r} J_1(\bar{\lambda}_n \tilde{r}) \left[\sum_{m=0}^{\infty} b_m \tilde{r}^{2m+1} \right] \mathrm{d}\tilde{r} \tag{67c}$$

The subscript sw indicates that these are the velocity perturbations due only to induced swirl. The velocity perturbations due to Stefan flow and to density variations can be added to these values. In the inviscid limit where $b_m = 0$, Eqs. (67a–67c) indicate that both the axial velocity and radial velocity perturbations will have zero value everywhere. In the viscous case with swirl, the axial velocity perturbation at $\tilde{x} = 0$ will be nonzero, whereas the radial velocity is zero there. Nonzero values can be expected for both velocity perturbations for the flow downstream of the entrance.

If we change the inflow conditions so that $u_{1\mathrm{sw}} = 0$ at $\tilde{x} = 0$ while the radial velocity is not constrained, Eqs. (67a) and (67b) remain unchanged, but Eq. (67c) is replaced by

$$\bar{c}_n = \frac{2}{k_1 \tilde{r}_i^2 J_0^2(\bar{\lambda}_n \tilde{r}_i)} \int_0^{\tilde{r}_i} \tilde{r} J_0(\bar{\lambda}_n \tilde{r}) \left[\sum_{m=0}^{\infty} (1+m) b_m \tilde{r}^{2m} \right] \mathrm{d}\tilde{r} \tag{67d}$$

Figure 14 presents the swirl-induced radial velocity component for a viscous plug-flow case with the value of $Re = 1000$. The radial velocity is positive everywhere and, therefore, can be expected to add to the transfer of heat to the liquid surface. It can also reduce the transfer of fuel vapor mass away from the surface. The radial velocity behaves similarly to the tangential velocity that induced it, namely, a maximum is obtained at some radial position and decay of magnitude with increasing downstream distance is obtained. Note that the homogeneous solutions of Eqs. (67a) and (67b) do not depend on downstream position through $\tilde{x}/Re$.

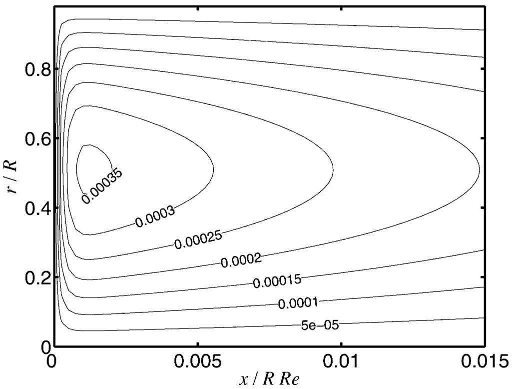

Fig. 14 Contours of nondimensional radial velocity component induced by swirl for $Re = 1000$, plug-flow axial velocity profile.

VIII. Stefan Flow and Effects of Gas Expansion

Another radial velocity component is created by the vaporization. This flow perturbation is known as the Stefan flow. The linear nature of the system of Eqs. (60) allows us to add the velocity perturbations. Because the vaporization rate per unit surface area $\dot{m} = -\rho_0 v_{1s}$, it follows from Eq. (41a) for the limiting case of plug flow that the Stefan flow component of radial velocity at the liquid/gas interface is

$$\frac{v_{1s}}{u_0[\nu Y_{O\infty} + Y_{Fs}]} = -\frac{2}{Pe} \frac{1}{\tilde{r}_i} \sum_{n=1}^{\infty} \exp(-k_n \tilde{x}) \tag{68}$$

The Stefan velocity at the interface is radially inward and thereby negative. In this limit, the velocity component becomes infinite at $\tilde{x} = 0$.

The preceding analyses have considered density to be constant. However, gas expansion will affect the velocity field and thereby affect transport and species conversion rates. Thus, in this section, the expansion effect is considered within the linearized framework.

The density $\rho = \rho_0 + \rho_1$ can be considered to be primarily dependent on the temperature, $T = T_\infty + T_1$. That is, the pressure is essentially uniform as far as thermodynamic importance, and molecular weight variations will not be considered. The subscript zero denotes the constant inflow values, whereas the subscript unity implies the perturbation due to heat release, transport, and expansion. A perfect gas relationship is assumed. Then, a linearized relation between density and temperature perturbations yields

$$\rho_1/\rho_0 = -T_1/T_\infty = -\left[\left(\alpha^{(1)}\big/c_p T_{0\infty}\right) - 1 + \delta_A\left(Q\alpha^{(2)}\big/c_p T_{0\infty}\right)\right] \tag{69}$$

The Shvab-Zel'dovich variables definitions have been used to obtain the second relation. On the fuel side of the flame $\delta_A = 0$, whereas on the air side $\delta_A = 1$, that is, $\delta_A = H(-\alpha - Y_{FS})$ where H is the Heaviside function.

For combustion problems, the temperature and density perturbations will be larger than the zero-order values, causing a linear approximation to give a negative density. Therefore, we make an ad hoc nonlinear correction for the relationship between density and temperature perturbations. Now, Eq. (69) is replaced by

$$\frac{\rho_1}{\rho_0} = -\frac{T_1}{T_\infty} \frac{1}{1 + T_1/T_\infty} = -\frac{\left[\left(\alpha^{(1)}\big/c_p T_\infty\right) - 1 + \delta_A\left(Q\alpha^{(2)}\big/c_p T_\infty\right)\right]}{\left[\left(\alpha^{(1)}\big/c_p T_\infty\right) + \delta_A\left(Q\alpha^{(2)}\big/c_p T_\infty\right)\right]} \tag{70}$$

Now, modify Eq. (16) by subtracting the $\tilde{x}$ derivative of a function of $\tilde{r}$, which, of course, is zero. That is, ρ_0 is constant, and u_0 is a function of $\tilde{r}$ for parabolic base flow and a constant for plug flow. Thus, we may state

$$\frac{\partial}{\partial \tilde{x}}(\rho u - \rho_0 u_0) + \frac{1}{\tilde{r}} \frac{\partial}{\partial \tilde{r}}(\rho v \tilde{r}) = 0 \tag{71}$$

and $\rho u = \rho_0 u_0$ at the inflow plane $\tilde{x} = 0$. The radial velocity is zero at the centerline and equal to $v_{1s}(\tilde{x})$ at the film interface, $\tilde{r} = \tilde{r}_i$. The following exact solution to this continuity equation can be found by inspection:

$$\frac{\rho u}{\rho_0 u_0} = 1 - 2\left(\frac{\rho_s}{\rho_0 \tilde{r}_i}\right) \int_0^{\tilde{x}} \left(\frac{v_{1s}(\tilde{x}')}{u_0}\right) \mathrm{d}\tilde{x}', \qquad \frac{\rho v}{\rho_0 u_0} = \frac{\rho_s v_{1s}(\tilde{x}) \tilde{r}}{\rho_0 u_0 \tilde{r}_i} \tag{72}$$

In these equations, $\rho = \rho_0 + \rho_1$, where ρ_1 is determined by Eq. (70) and $v_{1s}(\tilde{x})$ is given by Eq. (68). Note that this solution can only apply when the inflow condition for the radial velocity gives a linear profile. Furthermore, it implies that ρu is function only of one variable $\tilde{x}$ and is independent of radial position. The density and axial velocity themselves can depend on both spatial variables.

The inviscid-gas-flow (large Reynolds number) assumption is made in this section. The Peclet number is considered to be finite in the determination of the density field so that negligible Prandtl number is implied, a very strong but convenient assumption. For the inviscid plug flow without any radial velocity component at the inflow, the radial velocity due to swirl is zero everywhere. The pressure field due to the Stefan flow and the varying density can be determined by integration of the two linearized momentum equations. In the infinite Reynolds number limit (inviscid plug flow), Eqs. (61b) and (61c) become

$$\frac{\partial}{\partial \tilde{x}}\left(\frac{u_1}{u_0}\right) + \frac{\partial}{\partial \tilde{x}}\left(\frac{p_1}{\rho_0 u_0^2}\right) = 0, \qquad \frac{\partial}{\partial \tilde{x}}\left(\frac{v_1}{u_0}\right) + \frac{\partial}{\partial \tilde{r}}\left(\frac{p_1}{\rho_0 u_0^2}\right) = 0 \tag{73}$$

Equation (72) would provide the velocity values for these equations. Equations (73) can each be differentiated and then added together. Note the first equation is differentiated with respect to $\tilde{x}$, whereas the second equation is multiplied by $\tilde{r}$, then differentiated with respect to $\tilde{r}$, and finally divided by $\tilde{r}$ before adding the two equations. Equation (60a) can be used to eliminate the velocity perturbation terms. The result is a Poisson equation for the pressure perturbation,

$$\tilde{\nabla}^2 p_1 = u_0^2 \frac{\partial^2 \rho_1}{\partial \tilde{x}^2} \tag{74}$$

If the determination of the pressure perturbation is desired, the right side can be evaluated using Eq. (70), and a Green's function (see Ref. 32) can be created to obtain the solution. The boundary conditions on the normal pressure gradient at the inflow and exit planes and at the liquid surface can be obtained by applying Eq. (73) at those boundaries.

When we specify the inputs for the calculations of the Stefan velocity and the expansion velocity, the quantities $Q/c_p T_\infty$, Y_{Fs}, and $[\nu Y_{O\infty} + Y_{Fs}]$ will depend on the particular fuel/oxidizer combination. We use here heptane and air.

The variation of the nondimensional density perturbation throughout the combustion chamber is shown in Fig. 15 for the case $Pe = 500$, whereas the corresponding results for the velocity perturbations due to the combined effects of vaporization and density variation are shown in Figs. 16 and 17. The inflow-air temperature is 298 K, whereas the heptane liquid surface is at the wet-bulb value of about 360 K. The contours are shown as a a function of $\tilde{x}/Pe$ because the dependence on the two variables $\tilde{x}$ and Peclet number collapse to that similarity variable for large values of Peclet number. Also, as indicated through Eq. (68), the asymptotic behavior for the radial velocity is indicated by plotting contours of the product $(v_1/u_0)Pe$. The density perturbation in Fig. 15 has its most negative value (a minimum) at the flame. The axial velocity perturbation is closely correlated with the density perturbation and achieves a maximum value at the flame. Because the product of density and radial velocity is proportional to the radial position and density has a minimum value at the flame, the negative (inward) radial velocity has a maximum absolute value in its radial variation at a point near the flame.

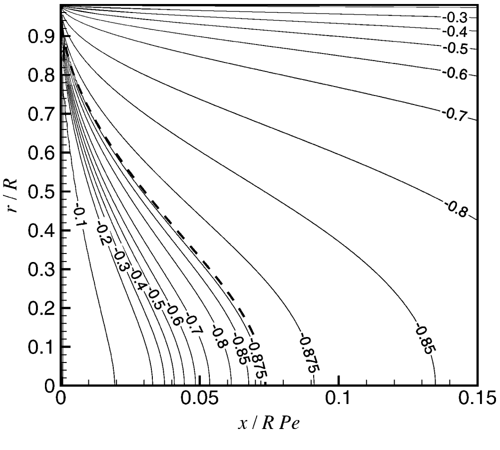

Fig. 15 Contours of the nondimensional density perturbation variation in combustor with inviscid plug flow, *Pe* = 500.

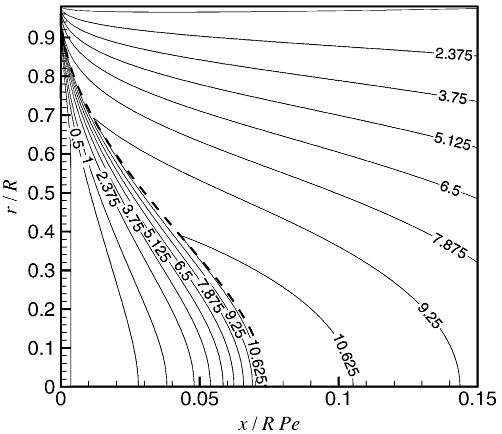

Fig. 16 Contours of nondimensional axial velocity perturbation due to vaporization and density variation with inviscid plug flow, *Pe* = 500.

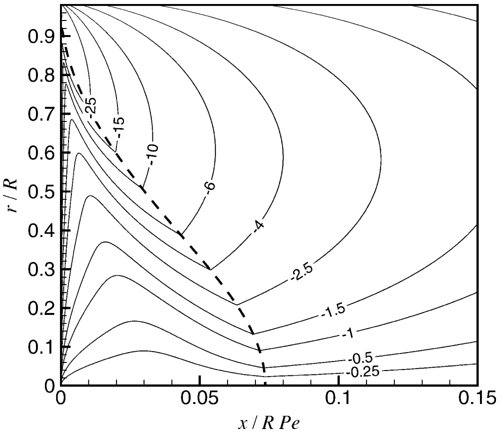

Fig. 17 Contours of product of Peclet number and nondimensional radial velocity perturbation due to vaporization and density variation with inviscid plug flow, *Pe* = 500.

Now the three components of the radial velocity due to swirl, vaporization, and gas expansion can be summed using Eqs. (67b) and (72) to give the total radial velocity,

$$v_{1\text{tot}}/u_0 = (v_{1\text{sw}}/u_0) + (v_{1st}/u_0) + (v_{1e}/u_0) \tag{75}$$

Unfortunately, in the inviscid situation studied for the Stefan flow and gas-expansion-induced flow, the radial velocity perturbation due to swirl is zero. In other cases, its magnitude and effect on transport is likely to be significant.

IX. Correction on Transport, Vaporization, and Burning Rates Due to Radial Velocity

The solutions for the scalar variables and for the vaporization rates given by Eqs. (33) and (37–41) will be modified by the effects of the radial velocity. The governing equation (27) must be modified.

The general equation for the scalar variable can be written in dimensional form as

$$L(\alpha^{1,2}) = \rho D \nabla^2 \alpha^{1,2} - \rho \boldsymbol{u} \cdot \nabla \alpha^{1,2} = 0 \tag{76}$$

The definition of the Peclet number for this variable density case is generalized with $\rho D = \text{constant}$. That is, $Pe = \rho_0 u_0 R/\rho D$. In the constant density case, it collapses to the earlier definition.

The nondimensional form for the infinite Reynolds number (plug-flow) limit becomes

$$\tilde{\nabla}^2\alpha - Pe\frac{\rho\boldsymbol{u}}{\rho_0 u_0}\cdot\tilde{\nabla}\alpha = \tilde{\nabla}^2\alpha - Pe\left[\frac{\rho u}{\rho_0 u_0}\frac{\partial\alpha}{\partial\tilde{x}} + \frac{\rho v}{\rho_0 u_0}\frac{\partial\alpha}{\partial\tilde{r}}\right] = 0 \quad (77)$$

We can take advantage of the situation here with ρu being a function only of $\tilde{x}$ according to Eq. (72). Define $a(\tilde{x}) = Pe(\rho u/\rho_0 u_0)$ and $b(\tilde{r}, \tilde{x}) = Pe(\rho v/\rho_0 u_0)$. Now, Eq. (77) can be replaced by

$$\tilde{\nabla}^2\hat{\alpha} - a(\tilde{x})\frac{\partial\hat{\alpha}}{\partial\tilde{x}} - b(\tilde{r}, \tilde{x})\frac{\partial\hat{\alpha}}{\partial\tilde{r}} = 0 \quad (78)$$

Equation (78) can be solved by numerical integration. Simultaneous solution with Eqs. (72) is required.

The boundary conditions for Eq. (78) can now be set. Along the axis of symmetry, the boundary condition is

$$\frac{\partial\alpha}{\partial\tilde{r}}(0, \tilde{x}) = 0 \quad (79)$$

At the liquid surface, we have that

$$\alpha(\tilde{r}_i, \tilde{x}) = 0 \quad (80)$$

At the inflow plane, we have

$$\alpha(\tilde{r}, 0) = 1 \quad (81)$$

At the exit plane after combustion is completed, it can be stated that the $\tilde{x}$ derivative of the variable α goes to zero,

$$\frac{\partial\alpha}{\partial\tilde{x}}\left(\tilde{r}, \frac{L}{R}\right) = 0 \quad (82)$$

After solving Eqs. (78–82) for α, we can calculate the transport rates and vaporization rate at the liquid surface, in particular, we have

$$\frac{\partial\alpha}{\partial\tilde{r}}(\tilde{r}_i, \tilde{x}) = \frac{R}{\alpha_0}\frac{\partial\alpha^{(1,2)}}{\partial r}(R_i, x) = \frac{\dot{m}R}{\rho D\alpha_0/(1 - Y_{Fs})} \quad (83)$$

Equation (78) with the boundary conditions (79–82) was solved by finite difference calculations for heptane fuel and air combustion at various Peclet number values. Central differencing was used to discretize the spatial derivatives. Although the use of central differencing circumvents the problem of numerical diffusion, cell Reynolds (or Peclet) numbers were monitored and underrelaxation was employed to provide stability and accuracy. For Peclet numbers greater than 100, at least 400 nodes were used in the axial and radial directions. Numerical parameter changes were performed to ensure grid independence and accuracy. Computations with high Peclet numbers required about one day on a single processor desktop computer.

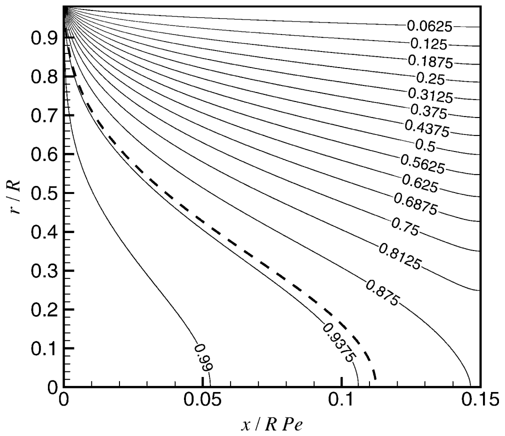

Fig. 18 Corrected α scalar contours due to velocity perturbations, *Pe* = 10, plug flow.

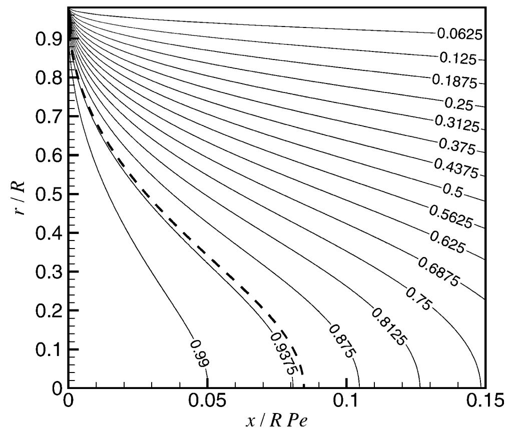

Fig. 19 Corrected α scalar contours due to velocity perturbations, *Pe* = 100, plug flow.

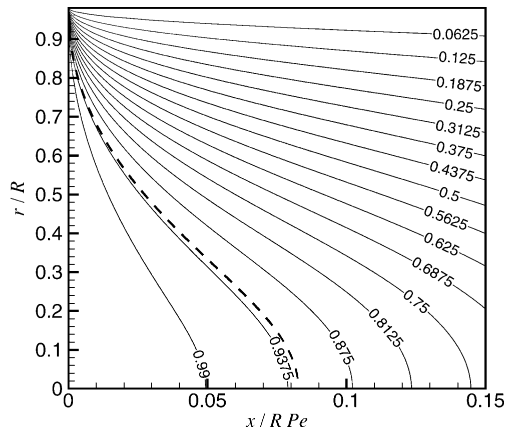

Fig. 20 Corrected α scalar contours due to velocity perturbations, *Pe* = 500, plug flow.

Figures 18–20 show the corrected results for the scalar α at the three values, $Pe = 10$, 100, and 500, respectively, with plug flow. The combined effects of vaporization and density variation do tend to distort the contours as compared to the uncorrected case. A contour line near the liquid film is moved away from the film by the Stefan flow. The point where the contour crosses the symmetry axis is moved downstream because the stream moves faster due to both the added mass from vaporization and the expansion due to temperature variation. The contours are plotted with the axial coordinate normalized by Peclet number because for very large Peclet values, the dependencies on Peclet number and the axial coordinate are expected to collapse accordingly, as mentioned earlier. In the range from 10 to 500, some additional dependency on Peclet number is seen; the differences between the $Pe = 10$ and 100 cases are greater than the differences between the 100 and 500 cases. This can be seen in Figs. 21 and 22, where the flame contour and the normalized transport rate at the liquid surface with a heptane–air flow are compared for the three Peclet numbers. Furthermore, the corrected and uncorrected values are compared. For the larger Peclet number, the correction due to Stefan flow reduces the transport rate at the film surface so that a longer film length will be required to supply the required amount of fuel vapor.

Comparisons of the flame contour are also shown in Fig. 23; the effects of axial diffusion and the effects of the correction due to vaporization and density variation are shown for the $Pe = 10$ case. Axial diffusion effects are eliminated from the uncorrected scalar solution by using Eqs. (33) and (36) after setting $\lambda^2 \equiv Pek$. Those axial diffusion effects are eliminated from the corrected solutions by replacing the Laplacian operator in Eq. (78) with only the radial

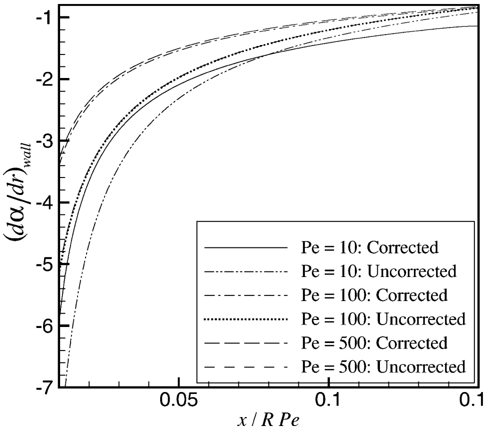

Fig. 21 Corrected and uncorrected nondimensional transport rates at liquid surface, with heptane.

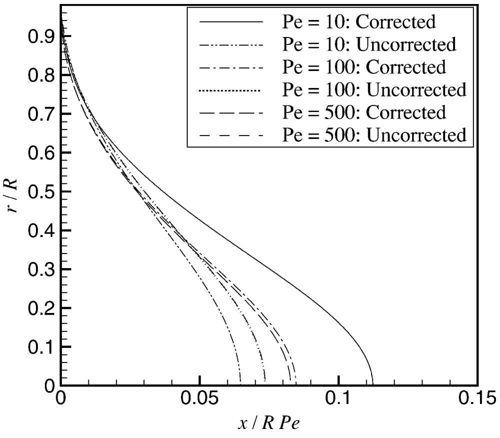

Fig. 22 Corrected and uncorrected flame shapes at various Peclet numbers for plug flow, with heptane.

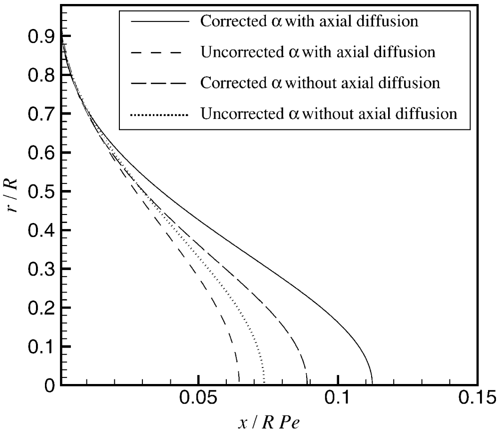

Fig. 23 Flame position with and without axial diffusion, plug flow, *Pe* = 10.

derivatives and excluding the axial second derivative; consistently, the exit-boundary condition given by Eq. (82) is eliminated. For this value of Peclet number, the effect on the solution and on flame position is significant; for very large Peclet number, the axial diffusion effects are negligible. For the uncorrected solution, the axial diffusion increases the burning rate per unit length and shortens flame length. Apparently, the axial diffusion brings the reactants to the flame faster. However, this increased burning intensity will also increase the vaporization rate per unit length. Therefore, for the corrected solution, an increase in axial velocity at a given downstream position will result; this means that the corrected flame with axial diffusion stretches farther downstream than the corrected flame solution without axial diffusion.

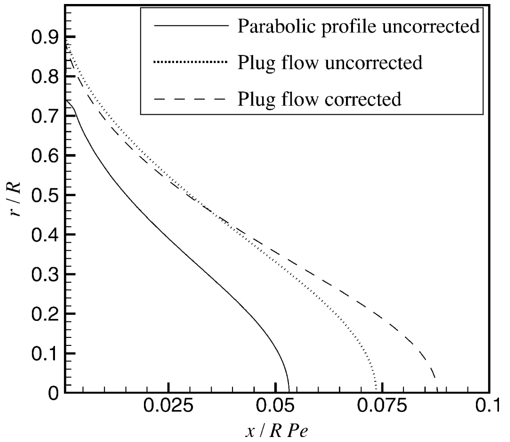

Fig. 24 Comparisons of flame contours for three types of solutions, *Pe* = 500.

Figure 24 shows the differences in the flame contour results at $Pe = 500$ for three types of calculation. The plug flow results in a longer flame, whereas again the corrections due to the velocity perturbations also result in a longer flame. The longer flame for the plug flow is attributed to the higher average axial velocity for a given Peclet number value.

X. Conclusions

The liquid-film combustor has been analyzed for steady, laminar, axisymmetric flow for the two cases of a fully developed parabolic velocity profile and a flat plug-flow velocity profile to describe the base flow. Linear perturbations have been used to treat the effects of swirl-induced flow, vaporization-induced flow, and gas expansion. A solution with a standing diffusion flame and cool walls is obtained, in qualitative agreement with experiments. Thus, theoretical support is given to the experimental observation that, unlike premixed combustion or spray combustion, stable liquid-fuel film burning can occur in small-diameter chambers without quenching. In particular, the vaporizing liquid film allows the wall temperatures to remain below the liquid boiling point.

The flame length at higher Peclet number values is many combustor radii and is also substantially longer than the film length required for vaporizing a stoichiometric amount of fuel. This situation can result in dry walls exposed to high heat fluxes. This means that, for higher mass flows, it is desirable to increase significantly the effective diffusivity (to decrease the effective Peclet number and flame length) via vortex generation.

The perturbations to the velocity field due to vaporization and gas expansion have significant effects on the combustion process, extending the flame length and modifying the vaporization rate per unit surface area as a function of downstream position.

For the inviscid flow, swirl has no effect within this linear theory. This linearized analysis gives some indication of the important physics and of some length scales of the flow downstream of the air inlet; however, it can not represent well the inflow and flame holding details. The swirling inflow would have a three-dimensional character and would typically involve jets from ports, wakes of flows through vanes, and/or recirculation zones. Computational fluid dynamic methods are required to give better resolution of all of the physics in the inflow and flame holding region. Therefore, three-dimensional solutions of the Navier–Stokes equation for the multicomponent reacting flow are required in the future for resolution of this upstream region.

Acknowledgment

This research has been supported by National Science Foundation Grant CTS-0212163 with Farley Fisher and, later, Linda G. Blevins as Program Directors.

References

[1] Waitz, I. A., Gauba, G., and Tzeng, Y.-S., "Combustors for Micro-Gas Turbine Engines," *Journal of Fluids Engineering*, Vol. 120, No. 1, 1998, pp. 109–117.

[2] Fu, K., Knobloch, A., Martinez, F., Walther, D. C., Fernandez-Pello, A. C., Pisano, A., Liepmann, D., Miyasaka, K., and Maruta, K., "Design and Experimental Results of Small-Scale Rotary Engines," *Proceedings of the 2001 International Mechanical Engineering Congress and Exposition (ICECE)*, American Society of Mechanical Engineers, 2001, New York.

[3] Micci, M. M., and Ketsdever, A. D. (eds.), *Micropropulsion for Small Spacecraft*, Vol. 187, Progress in Astronautics and Aeronautics, AIAA, Reston, VA, 2000.

[4] Lindsay, W., Teasdale, D., Milanovic, V., Pister, K., and Fernandez-Pello, A. C., "Thrust and Electrical Power from Solid Propellant Microrockets," *MEMS 2001, 14th IEEE International Conference on Micro Electro Mechanical Systems*, 2001, pp. 606–610.

[5] Ahn, J., Eastwood, C., Sitzki, L., and Ronney, P. D., "Gas-Phase and Catalytic Combustion in Heat-Recirculating Burners," *Proceedings of the Combustion Institute*, Vol. 30, 2004, pp. 2463–2472.

[6] Chao, Y.-C., Chen, G.-B., and Tsai, M.-H., "Investigation of the Performance Characteristics of a Miniature Catalytic Gas Turbine Combustor," *4th Pacific International Conference on Aerospace Science and Technology*, 2001.

[7] Kyritsis, D. C., Guerrero-Arias, I., Roychoudhury, S., and Gomez, A., "Mesoscale Power Generation by a Catalytic Combustor Using Electrosprayed Liquid Hydrocarbons," *Proceedings of the Combustion Institute*, Vol. 29, 2002, pp. 965–972.

[8] Fernandez-Pello, A. C., "Micropower Generation Using Combustion Issues and Approaches," *Proceedings of the Combustion Institute*, Vol. 29, 2002, pp. 883–899.

[9] Walther, D. C., and Fernandez-Pello, A. C., "Microscale Combustion: Issues and Opportunities," *Eastern States Section Combustion Institute Fall Technical Meeting*, Hilton Head, SC, Dec. 2001.

[10] Sirignano, W. A., Dunn-Rankin, D., Strayer, B., and Pham, T., "Miniature Combustor with Liquid-Fuel Film," *Proceedings of the Western States Section/Combustion Institute Fall Meeting*, Salt Lake City, UT, Oct. 2001.

[11] Sirignano, W. A., "Analysis of Miniature Liquid-Film Combustor," *Proceedings of the Eastern States Section/Combustion Institute Fall Meeting*, Hilton Head, SC, Dec. 2001.

[12] Pham, T. K., Dunn-Rankin, D., and Sirignano, W. A., "Further Developments of Miniature Fuel-Film Combustion Devices," *Proceedings of Western States Section/Combustion Institute Spring Technical Meeting*, San Diego, CA, March 2002.

[13] Sirignano, W. A., Pham, T. K., and Dunn-Rankin, D., "Miniature Scale Liquid-Fuel Film Combustor," *Proceedings of the Combustion Institute*, Vol. 29, 2002, pp. 925–931.

[14] Sirignano, W. A., *Fluid Dynamics and Transport Droplet and Sprays*, Cambridge Univ. Press, New York, 1999, Chap. 2.

[15] Sirignano, W. A., "A General Super-Scalar for the Combustion of Liquid Fuels," *Proceedings of the Combustion Institute*, Vol. 29, 2002, pp. 535–542.

[16] Emmons, H. W., "The Film Combustion of Liquid Fuel," *Zeitschrift für Angewandte Mathematik und Mechanik*, Vol. 36, No. 1/2, 1956, pp. 60–71.

[17] Smirnov, N. N., "Heat and Mass Transfer in a Multi-Component Chemically Reactive Gas Above a Liquid Fuel Layer," *International Journal of Heat and Mass Transfer*, Vol. 28, No. 5, 1985, pp. 929–938.

[18] Schiller, D. N., and Sirignano, W. A., "Mechanisms of Flame Spread Across Condensed Phase Fuels," *Physical and Chemical Aspects of Combustion, A Tribute to Irvin Glassman*, edited by F. L. Dryer and R. F. Sawyer, Combustion Science and Technology, Gordon and Breach, Amsterdam, 1997, pp. 353–407.

[19] Schiller, D. N., Sirignano, W. A., and Ross, H. D., "Computational Analysis of Flame Spread Over Alcohol Pools," *Combustion Science and Technology*, Vol. 118, No. 4–6, 1996, pp. 205–258.

[20] Schiller, D. N., and Sirignano, W. A., "Opposed-Flow Flame Spread Across n-Propanol Pools," *Proceedings of the Twenty-Sixth (International) Symposium on Combustion*, Combustion, Inst., Pittsburgh, 1997, pp. 1319–1325.

[21] Kim, I., and Sirignano, W. A., "Computational Study of Opposed-Forced-Flow Flame Spread Across Propanol Pools," *Combustion and Flame*, Vol. 132, No. 4, 2003, pp. 611–627.

[22] Kim, I., Schiller, D. N., and Sirignano, W. A., "Axisymmetric Flame Spread Across Propanol Pools in Normal and Zero Gravities," *Combustion Science and Technology*, Vol. 139, No. 1–6, 1998, p. 249.

[23] Cai, J., Lui, F., and Sirignano, W. A., "Three-Dimensional Flame Propagation Above Liquid Fuel Pools," *Combustion Science and Technology*, Vol. 174, No. 5–6 , 2002, pp. 5–34.

[24] Cai, J., Lui, F., and Sirignano, W. A., "Three-Dimensional Structures of Flames Over Liquid Fuel Pools," *Combustion Science and Technology*, Vol. 175, No. 11, 2003, pp. 2113–2139.

[25] Hoffman, K. A., Chiang, S. T., Siddiqui, S., and Papadakis, M., *Fundamental Equations of Fluid Mechanics,* Engineering Education Systems, Wichita, KS, 1996.

[26] Shah, R. K., and London, A. L., *Laminar Flow Forced Convection in Ducts*, Academic Press, New York, 1978.

[27] Drew, T. B., "Mathematical Attacks on Forced Convection Problems: A Review," *Transactions of the American Institute of Chemical Engineers*, Vol. 26, June 1931, pp. 26–80.

[28] Titchmarsh, E. C., *Eigenfunction Expansions Associated with Second-order Differential Equations. Part I*, Oxford, London, 1962.

[29] Churchill, R. V., *Fourier Series and Boundary Value Problems*, McGraw–Hill, New York, 1941, pp. 143–174.

[30] Papoutsakis, E., Ramkrishna, D., and Lim, H. C., "The Extended Graetz Problem with Prescribed Wall Flux," *AIChE Journal*, Vol. 26, No. 5, 1980, pp. 779–787.

[31] Papoutsakis, E., Ramkrishna, D., and Lim, H. C., "The Extended Graetz Problem with Dirichlet Wall Boundary Conditions," *Applied Scientific Research*, Vol. 36, No. 1, 1980, pp. 13–34.

[32] Morse, P. M., and Feshback, H., *Methods of Theoretical Physics*, pt. 1, McGraw–Hill, New York, 1953, pp. 832–869.